JOURNAL OF GEOPHYSICAL RESEARCH: OCEANS, VOL. 118, 4633–4661, doi:10.1002/jgrc.20305, 2013

# U.S. IOOS coastal and ocean modeling testbed: Evaluation of tide, wave, and hurricane surge response sensitivities to mesh resolution and friction in the Gulf of Mexico

P. C. Kerr,[1] R. C. Martyr,[1] A. S. Donahue,[1] M. E. Hope,[1] J. J. Westerink,[1] R. A. Luettich Jr.,[2] A. B. Kennedy,[1] J. C. Dietrich,[3] C. Dawson,[3] and H. J. Westerink[1]

Received 15 March 2013; revised 21 June 2013; accepted 5 July 2013; published 19 September 2013.

[1] This paper investigates model response sensitivities to mesh resolution, topographical details, bottom friction formulations, the interaction of wind waves and circulation, and nonlinear advection on tidal and hurricane surge and wave processes at the basin, shelf, wetland, and coastal channel scales within the Gulf of Mexico. Tides in the Gulf of Mexico are modestly energetic processes, whereas hurricane surge and waves are highly energetic. The unstructured-mesh, coupled wind-wave and circulation modeling system, SWAN+ADCIRC, is implemented to generate modeled tidal harmonic constituents and hurricane waves and surge for a Hurricane Ike (2008) hindcast. In the open ocean, mesh resolution requirements are less stringent in achieving accurate tidal signals or matching hurricane surge and wave responses; however, coarser resolution or the absence of intertidal zones decreases accuracy along protected nearshore and inland coastal areas due to improper conveyance and/or lateral attenuation. Bottom friction formulations are shown to have little impact on tidal signal accuracy, but hurricane surge is much more sensitive, especially in shelf waters, where development of a strong shore-parallel current is essential to the development of Ike's geostrophic setup. The spatial and temporal contributions of wave radiation stress gradients and nonlinear advection were charted for Ike. Nonlinear advection improves model performance by capturing an additional 10–20 cm of geostrophic setup and increasing resonant cross-shelf waves by 30–40 cm. Wave radiation stress gradients improve performance at coastal stations by adding an extra 20–40 cm to water levels.

**Citation:** Kerr, P. C., R. C. Martyr, A. S. Donahue, M. E. Hope, J. J. Westerink, R. A. Luettich Jr., A. B. Kennedy, J. C. Dietrich, C. Dawson, and H. J. Westerink (2013), U.S. IOOS coastal and ocean modeling testbed: Evaluation of tide, wave, and hurricane surge response sensitivities to mesh resolution and friction in the Gulf of Mexico, *J. Geophys. Res. Oceans*, *118*, 4633–4661, doi:10.1002/jgrc.20305.

## 1. Introduction

[2] Coastal and ocean models that simulate the complex and multiscale processes of tides, hurricane surge, and waves seek to balance cost and accuracy, which are functions of domain size, resolution, and incorporated physics. These implementation options, along with frictional parameterization, have the potential to affect model response. The Southeastern Universities Research Association (SURA)-led U.S. Integrated Ocean Observing System (IOOS)-funded Coastal Inundation Modeling Testbed (COMT) aims to evaluate and improve models already in operational use, as well as to facilitate the transition of additional models to operational use. As part of that objective, this study seeks to address model response sensitivities to these aspects of model design by evaluating them with a tidal constituent analysis and a hindcast of Hurricane Ike (2008) using the unstructured coupled wind-wave and circulation modeling system, SWAN+ADCIRC. Model response sensitivities to mesh resolution, bottom friction formulations, nonlinear advection, and wind waves, are investigated at the basin, shelf, wetland, floodplain, and channel scales within the Gulf of Mexico.

[3] An intermodel comparison of leading storm surge models was performed as part of the aforementioned testbed on the moderately resolved unstructured The ULtralite-Levee-Removed (ULLR) mesh for tides and hurricanes [*Kerr et al*., 2013a]. Popular circulation models, the ADvanced CIRCulation model (ADCIRC) [*Luettich et al*., 1992], Finite Volume Coastal Ocean Model (FVCOM) [*Chen et al*., 2003], and the Semi-implicit Eulerian Lagrangian Finite Element model (SELFE) [*Zhang and Baptista*, 2008], performed

Additional supporting information may be found in the online version of this article.

[1]Department of Civil and Environmental Engineering and Earth Sciences, University of Notre Dame, Notre Dame, Indiana, USA.
[2]Institute of Marine Sciences, University of North Carolina at Chapel Hill, Chapel Hill, North Carolina, USA.
[3]Institute for Computational Engineering and Sciences, University of Texas at Austin, Austin, Texas, USA.

Corresponding author: P. C. Kerr, Department of Civil and Environmental Engineering and Earth Sciences, University of Notre Dame, 156 Fitzpatrick Hall, Notre Dame, IN 46556, USA. (PCorbittKerr@gmail.com)


2169-9275/13/10.1002/jgrc.20305

similarly and fairly well on the ULLR mesh. The resolution of the ULLR is considerably less than the resolution of SL18TX33 used by *Hope et al*. [2013] in their comprehensive hindcast of Ike, which achieved better overall error statistics than the COMT models on the ULLR mesh. This leads to the uncertainty as to the effect higher resolution and its spatial distribution have on model response and accuracy. Many of the issues addressed in this study stemmed from questions that arose as part of the testbed.

[4] SL18TX33 is the most recent unstructured mesh in a series of mesh evolutions that have occurred over the past two decades as part of an effort to improve hurricane storm surge and wave modeling in the Gulf of Mexico using ADCIRC and eventually SWAN+ADCIRC. These unstructured meshes have used progressively more resolution to describe the coastal ocean, as shown in the increase of triangular elements and vertices (nodes). *Westerink et al*. [1994] and *Blain et al*. [1994] presented a 23,711 node (and 41,709 element) unstructured, triangular mesh that encompassed the Gulf of Mexico, Caribbean Sea, and Atlantic Ocean out to the 60°W meridian, which was used to study tides and Hurricane Kate (1985). The domain was selected to minimize the influence of the domain boundary on model response. *Blain et al*. [1998] presented the SG01 (23,566 nodes and 43,238 elements) and CG01 (90,435 nodes and 179,952 elements) meshes to demonstrate that insufficient mesh resolution in deep water leads to sizable underprediction errors, and under-resolution in shallow areas leads to overprediction errors, for a hindcast of Hurricane Camille (1969). *Mukai et al*. [2002] presented the EC2001 (254,629 nodes and 492,182 elements) mesh with increased resolution throughout the domain and developed a highly skillful tidal atlas, which is used in this study. In contrast to these previous studies, which used a no normal flow shoreline boundary, *Westerink et al*. [2008] introduced S08 (314,442 nodes and 600,331 elements), which expanded the domain into southern Louisiana's floodplain and featured levees and improved resolution of hydraulic features such as rivers and channels, and was used to hindcast Hurricanes Betsy (1965) and Andrew (1992). *Bunya et al*. [2010] and *Dietrich et al*. [2010] presented hindcasts of Hurricanes Katrina and Rita (2005) using SL15 (2,409,635 nodes and 4,721,496 elements), with expanded Louisiana and Mississippi coverage and significantly higher resolution across the Gulf, shelf, floodplain, and river scales. A notable advancement to this mesh was the introduction of a spatially varying bottom friction coefficient. While noticeable improvements in model performance were made with each mesh advancement, it was also important that there was considerable growth of bathymetric, topographic, and land-use data to inform the models, as well as observational data that could be used to validate and lend further insight into physical processes and thus model design.

[5] To address less than ideal performance for a hindcast of Hurricane Gustav (2008) at the river, floodplain, and shelf scale, SL16 (5,035,113 nodes and 9,945,623 elements) was developed with higher resolution in the Mississippi River and Gulf [*Dietrich et al*., 2011a]. For the hindcast of Ike, *Kennedy et al*. [2011] introduced TX2008_R33 (3,323,388 nodes and 6,674,415 elements), which featured the omission of the southern Louisiana and Mississippi coastal floodplain from SL16 and the addition of the Texas coastal floodplain, bays, lakes, and channels. SL18TX33 (9,108,128 nodes and 18,061,765 elements) represents the most complete northern Gulf Coast mesh to date. It features the high resolution of the Texas coastal floodplain from TX2008_R33 and the high resolution of the Louisiana-Mississippi coastal floodplain from SL16, along with increased resolution in western Louisiana and in the Atchafalaya River system. The SL18TX33 mesh also has increased resolution of the Florida Gulf Coast to include the intertidal zones, wetlands, and bays. The merging of the southern Louisiana and Texas meshes was performed due to the very large geographic coastal region that was affected by Ike [*Hope et al*., 2013].

[6] Previous studies have been performed on the design of shallow water model meshes to meet numerical stability constraints and minimize truncation errors [e.g., *Westerink et al*., 1994; *Blain et al*., 1998; *Hagen et al*., 2001], but few have performed evaluations of the sensitivity of both tidal and hurricane responses and performance at different resolutions. This study seeks to address the degree to which mesh resolution influences model accuracy, and infer from a simple comparison of simulations using high and moderately resolved meshes, where and why it is needed. *Mukai et al*. [2002] and *Bunya et al*. [2010] conducted Gulf of Mexico tidal validation studies using the ADCIRC model on the EC2001 and SL15 meshes, respectively; however, neither investigated the extent to which mesh resolution affected tidal accuracy. To explore the impact of mesh resolution on tidal accuracy, the results of tidal simulations using ADCIRC on the moderate-resolution ULLR and high-resolution SL18TX33 meshes were analyzed for 82 stations within the Gulf of Mexico and model response sensitivity was categorically addressed by constituent and geographic location. In the open ocean, mesh resolution requirements are shown to be less stringent in achieving accurate tidal signals; however, in protected and inland areas, higher resolution dramatically increases accuracy for tidal signals because propagation through narrow conveyances and attenuation plays an important role in accurately capturing these tidal dynamics.

[7] A current trend in storm surge modeling is the coupling of circulation and nonphase resolving wave models on the same mesh; therefore, model response sensitivity to mesh resolution is very topical considering the need to ensure that jointly used meshes have enough resolution to accurately capture both circulation and wave physics, their interactivity, and their diverse range of scales. This study utilized the popular and highly validated SWAN+ADCIRC coupled circulation and wave model to explore mesh resolution sensitivity to hurricane flows for Hurricane Ike (2008). This storm was chosen due to its large geographic scale, its complexity, its wide range of hurricane physics, and its wealth of collected observation data. Based on qualitative and quantitative comparisons of model to measured data, higher resolution was found to have very little influence on accuracy of wave characteristics and water levels in the open Gulf, but it became increasingly important further inland for water levels. Coarser resolution decreases the accuracy of surge propagation and attenuation. For example, an artificial retardation of surge through lack of conveyance can lead to lower levels further inland and higher surge levels nearer to the coast.

[8] Empirical formulations for wind-sea and bottom-current interactions are often the most critiqued components

of coastal and ocean models due to the lack of demonstrated universal forms for these relationships and their coefficients. Despite this limitation, parameterizations of these physics are commonly applied. Recent storm surge studies [e.g., *Bunya et al*., 2010; *Dietrich et al*., 2011a; *Hope et al*., 2013] have applied data-driven wind-sea drag laws, as well as bottom friction values based on bottom type, with good success. The present study examines the effects of bottom friction formulation on currents for both low and high energy events in the Gulf and found that a limited drag coefficient formulation had little impact on tidal signal accuracy, but hurricane surge was much more sensitive, especially in shelf waters, where development of a strong shore parallel current is essential to the development of Ike's geostrophic setup as explored by *Kennedy et al*. [2011]. This present study also explores model response sensitivity to bottom friction formulations in SWAN and shows that for this particular application, Madsen and JONSWAP (Joint North Sea Wave Project) formulations perform similarly and skillfully, but that the JONSWAP bottom friction coefficient, which appeared to yield the best results for the smooth shelf of the Louisiana-Texas Gulf was 0.019 $m^2/s^3$, instead of the 0.038 $m^2/s^3$ suggested by *Hasselmann et al*. [1973] in their study of the North Sea.

[9] Some coastal and ocean models utilize a no normal flow shoreline boundary because it omits the need for wet/dry logic and decreases model size, or because coastal inundation is not the primary interest. A shoreline boundary acts as a wall to shore-perpendicular currents and neglects the intertidal zone area and inundated coastal floodplain, whereas, in reality, shore-perpendicular currents can push inland and allow for attenuation of shoreward signals. The present study shows that intertidal zones and/or coastal floodplain inundation decreases tidal amplitudes and lower surge levels in both coastal and inland coastal waters. This effect is not as striking along the open coast, but in inland bays and estuaries, the damping of signals through attenuation is significant.

[10] The National Hurricane Center's operational forecast model, Sea, Lake, and Overland Surges from Hurricanes model (SLOSH), does not simulate tides, waves, or nonlinear advection [*Jelesnianski et al*., 1992], which are all components that were suggested by *Hope et al*. [2013] to be contributing processes to Ike's hydrodynamics. Because certain processes or physical components are not always used, the present study seeks to justify the importance of their contributions by isolating the spatial and temporal contributions of wave radiation stress gradients and nonlinear advection for an Ike hindcast. Nonlinear advection improves model performance by capturing an additional 10–20 cm of geostrophic setup and increasing resonant cross-shelf waves by 30–40 cm. Wave-radiation stress gradients improve performance at coastal stations by adding an extra 20–40 cm to water levels. In addition to waves and advection, the relative contributions of other components of the shallow water equations, such as bottom friction, wind stress, pressure, and Coriolis effect are temporally evaluated relative to each other at select locations in the Gulf to illustrate what and how components contributed during the progression of Ike.

### 1.1. Tides in the Gulf of Mexico

[11] Tides in the Gulf of Mexico are a moderately energetic process. Tides propagate into the semienclosed Gulf from the western Atlantic Ocean and the Caribbean Sea via the Florida Straits and Yucatan Channel, respectively, and are also generated through local tidal potential forcing within the Gulf [*Mukai et al*., 2002; *Westerink et al*., 2008]. There is considerable uniformity in diurnal tidal constituent amplitudes and phases within the Gulf. This has been attributed to the cooscillation through the Florida Straits and Yucatan Channel and the weak contribution from local tidal potential forcing [*Gouillon et al*., 2010]. Semidiurnal tides are dominated by a basin scale amphidrome and strong amplification on the Florida and Louisiana-Texas shelves, and are significantly affected by the local tidal potential forcing. Tidal ranges in the Gulf of Mexico are approximately 0.5–1 m. The $M_2$ constituent is the largest contributor along the Florida and Louisiana-Texas coasts, whereas the $O_1$ and $K_1$ are the strongest contributors along the Mississippi, Alabama, and eastern Louisiana coasts. The $M_2$, $S_2$, $O_1$, and $K_1$ constituents make up 90% of the tidal bulk in the region [*He and Weisberg*, 2002]. Capturing tidal physics correctly is an important part of storm surge models, as they contribute to overall water levels and currents during hurricanes.

### 1.2. Synopsis of Hurricane Ike (2008)

[12] Ike was a complex, large-scale storm that highlighted a variety of storm surge processes in the northern Gulf of Mexico. In southeastern Louisiana, persistent easterly and southeasterly winds drove surge into the passes and lakes around New Orleans and drove water from Chandeleur Sound into the marshes east of the Mississippi River. As these winds persisted, water encroached over the marshes until it was driven into the Mississippi River and trapped against the western bank of the levee system. Due to the resultant large surface water gradient across the Bird's Foot Delta, high currents developed between the delta and shelf break. Due to Ike's steady northwest track (Figure 1a) and broad wind field, the wide Louisiana-Texas (LATEX) continental shelf experienced moderate-strength unidirectional winds for several days prior to landfall. These sustained winds allowed for the development of a strong, shore-parallel current. This strong current resulted in a geostrophic setup that caused an early rise in water along the coast, known as a forerunner surge [*Kennedy et al*., 2011]. A key component to the development of the forerunner surge is the relatively smooth bottom of the LATEX shelf. Unlike the sandy west Florida shelf in the eastern Gulf of Mexico, the LATEX shelf is made up primarily of mud and silt [*Buczkowski et al*., 2006], allowing for the acceleration of a strong, large-scale current across the entire shelf. The long time scale of the development and persistence of the forerunner surge allowed for effective inland penetration of surge into coastal eastern Texas and southwestern Louisiana. Following its generation, the forerunner surge propagated down the wide Texas shelf as a discernible free wave. The free wave reached Corpus Christi, Texas, as Ike was making landfall at Galveston. As Ike made landfall, winds quickly transitioned on the LATEX shelf from shore-parallel to shore-normal, and due to the effective inland penetration of the forerunner surge, Ike's peak winds drove surge far inland, leading to the storm's maximum water levels. As winds weakened, water receded overland, out of coastal lakes and bays, and from

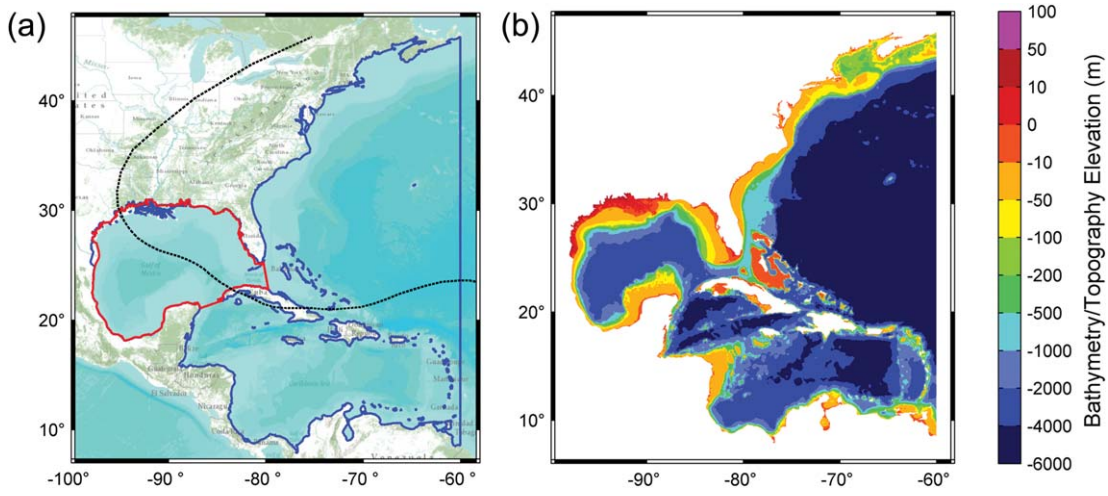


**Figure 1.** (left) Domain boundaries of ULLR (red), SL18TX33 (blue), and track of Ike (dashed black). (right) Bathymetry and topography in meters NAVD88 (2004.65) of SL18TX33.

the coast. When this coastal mass of water reached the abrupt continental shelf break, it was reflected back as an out-of-phase resonant wave. The initial cross-shelf wave and several recurrences can clearly be seen at several data stations across the coast [*Kennedy et al*., 2011]. The wave resonated with an approximate 12 h period, matching the resonant period of the LATEX shelf as evidenced by the amplification of semidiurnal tides on the shelf [*Hope et al*., 2013].

[13] In addition to the multitude of surge and circulation processes, Ike generated the largest data set to date of in situ water level time series, wave parameter time series, and still water high marks for a Gulf of Mexico tropical cyclone. This wealth of data provides an unprecedented opportunity to validate and evaluate numerical storm surge model performance over a large spatial scale examining surge and circulation processes ranging from the continental shelf to the channel scale.

## 2. Methods

### 2.1. Computational Models

[14] This study employed SWAN+ADCIRC [*Dietrich et al*., 2011b], an integral coupling of the Advanced Circulation (ADCIRC) model and the Simulating Waves Nearshore (SWAN) model. Hurricane simulations by *Dietrich et al*. [2011a, 2011b, 2012a] and *Hope et al*. [2013] have shown SWAN+ADCIRC to be an accurate, robust, and highly scalable coastal inundation, surge, and wind-wave model.

[15] ADCIRC, a continuous-Galerkin finite element model, solves for water levels using the generalized wave continuity equation (GWCE) and currents using the vertically integrated shallow water momentum equations (SWE) on an unstructured mesh [*Luettich et al*., 1992; *Dawson et al*., 2006; *Westerink et al*., 2008]. The SWE momentum equations are solved explicitly by ADCIRC, but the temporal discretization of the GWCE system is treated by a set of weighting control parameters, so it can be solved explicitly or implicitly. This study solved the GWCE in ADCIRC explicitly using the lumped mass matrix form of the GWCE [*Tanaka et al*., 2011].

[16] ADCIRC has shown good skill in simulating the complex response characteristics of the northern Gulf to hurricane and tidal forcing by utilizing unstructured meshes to resolve the basin, shelf, floodplain, and channel scales and by incorporating spatial frictional variability into the physical dissipation terms for circulation [*Bunya et al*., 2010]. Recent hurricane validation studies include Katrina (2005) and Rita (2005) using the SL15 mesh [*Bunya et al*., 2010; *Dietrich et al*., 2010], Gustav (2008) using the SL16 mesh [*Dietrich et al*., 2011a], and Ike (2008) using the TX2008_R33 mesh [*Kennedy et al*., 2011] and the SL18TX33 mesh [*Hope et al*., 2013].

[17] SWAN is a third-generation, phase-averaged wave model that simulates the evolution of wind-generated waves in inland waters, coastal regions, and the open ocean by solving the wave action balance equation for the wave action density spectrum [*Booij et al*., 1999]. The version of SWAN [*Zijlema*, 2010] employed here is designed to operate on the same mesh used by ADCIRC using a coupling mechanism that involves the transfer of wave radiation stress from SWAN to ADCIRC, and water levels, currents, and frictional roughness lengths from ADCIRC to SWAN at prescribed time intervals [*Dietrich et al*., 2011b].

### 2.2. Meshes

[18] This study features two unstructured triangular meshes: ULLR, a moderately resolved mesh [*Kerr et al*., 2013a] developed for the U.S. IOOS coastal and ocean modeling testbed; and SL18TX33, a finely resolved mesh [*Hope et al*., 2013]. The ULLR mesh covers the Gulf of Mexico, is tidally forced at open ocean boundaries along the Yucatan Channel and Florida Straits, and has river flux boundary conditions for the Atchafalaya and Mississippi Rivers. In contrast, the SL18TX33 mesh covers the western North Atlantic Ocean, the Gulf of Mexico, and the Caribbean Sea. It has an open ocean tidally forced boundary along the 60°W meridian and also has river flux boundary conditions for the Atchafalaya and Mississippi Rivers. The

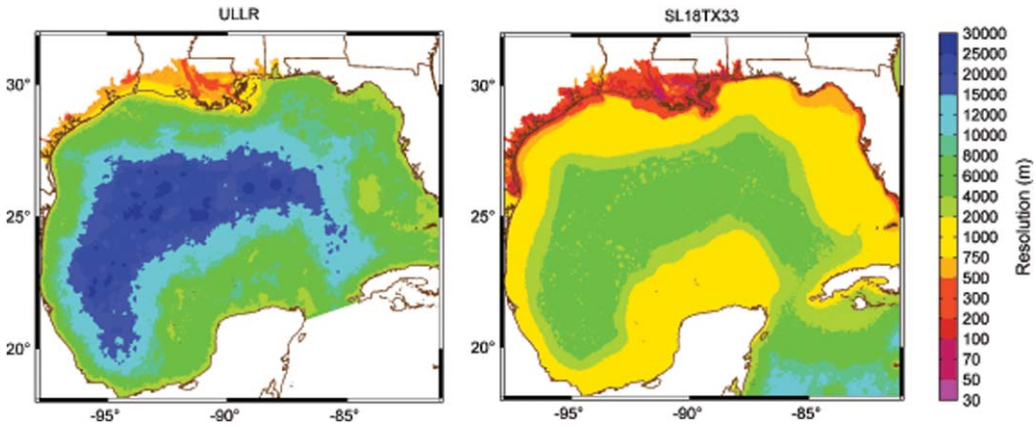


**Figure 2.** Grid resolution in meters within the Gulf of Mexico: (left) ULLR, (right) SL18TX33.

domain boundaries for these meshes and track of Ike are shown in Figure 1.

[19] The ULLR has 417,642 nodes (826,866 elements), whereas SL18TX33, with much higher resolution, has 9,288,245 nodes (18,300,169 elements). There is no uniform resolution scale between the two meshes (Figure 2 and Table 1). In general, SL18TX33 has 3–8 times the resolution of ULLR. In the Gulf, resolution ranges from 8–30 km for ULLR and 1–4 km for SL18TX33. On the LATEX shelf, the resolution is roughly 2–8 km for ULLR and 400–1000 m for SL18TX33. Resolution in the floodplains ranges from 500–2000 m for ULLR and 80–500 m for SL18TX33. *Martyr et al*. [2013] found that higher resolution in channels and rivers improved model response at capturing the faster moving currents that occur within these deeper and lower friction conduits; therefore, as shown in Figure 2, considerable attention has been paid in SL18TX33 to resolve these hydraulic features. Narrow inlets and channels within the floodplain and riverine basins are very highly resolved in SL18TX33 to accommodate the large flows that these channels transfer to the surrounding marshes and bays. In ULLR, some attention has been paid to resolve the Mississippi and Atchafalaya Rivers, but most other rivers and channels have been largely unaddressed due to the mesh's coarse resolution. The resolution at the river scale ranges from 100 to 500 m for ULLR and 30 to 80 m for SL18TX33. These significant mesh differences allow for a comparison of model responses to varying degrees of resolution.

### 2.3. Bathymetry and Topography

[20] The bathymetry and topography sources used in the construction of SL18TX33 and ULLR are identical to *Dietrich et al*. [2011a] in their synoptic study of Gustav and to *Hope et al*. [2013] in their synoptic study of Ike (Figure 1). Levees and roads that are obstacles to flood propagation are included in SL18TX33 as submesh scale weirs, but they were not included in ULLR. Levees along the Lower Mississippi River can contribute significantly to the generation of surge up the Mississippi River [*Kerr et al*., 2013b]. A precursor to the ULLR was created that included levees, but due to its coarse resolution, it was not possible to include as complete of a levee system as SL18TX33. Early simulations showed that levees combined with coarse riverine resolution overly constricted surge up the rivers and on the floodplain, and that a mesh without those levee features resulted in more realistic results. Levee and road heights and geographical positions are assigned from U.S. Army Corps of Engineers surveys and/or lidar databases.

[21] Water levels at the beginning of ADCIRC simulations are adjusted to account for the vertical datum, as well as seasonal variability in sea levels in the Gulf of Mexico. Simulations are referenced to the North American Vertical Datum of 1988, updated to the 2004.65 epoch, NAVD88(2004.65), by increasing water levels by 0.134 m at the beginning of the simulation [*Bunya et al*., 2010]. In addition, due to the seasonal variability of sea

**Table 1.** ULLR and SL18TX33 Meshes

| | ULLR | SL18TX33 |
|---|---|---|
| No. of Nodes | 417,642 | 9,228,245 |
| No. of Elements | 826,866 | 18,300,169 |
| Resolution | River: 100–500 m | River: 30–80 m |
| | Overland: 500–2000 m | Overland: 80–500 m |
| | Shelf: 2–8 km | Shelf: 400–1000 m |
| | Gulf: 8–30 km | Gulf: 1–4 km |
| Mississippi River Flow | 0 $m^3/s$ | Ike: 12,318 $m^3/s$ |
| Atchafalaya River Flow | 0 $m^3/s$ | Ike: 5,279 $m^3/s$ |
| Tidal Forcing | $O_1$, $K_1$, $Q_1$, $M_2$, $S_2$, $N_2$, $K_2$(EC2001v2e) | $O_1$, $P_1$, $K_1$, $Q_1$, $M_2$, $S_2$, $N_2$, $K_2$(TPXO7.2) |
| | $P_1$ (TPXO7.2, FES95.2) | |
| Open Ocean Boundary | Yucatan Channel and Florida Straits | 60°W longitude |
| Levees | No | Yes |

level in the Gulf caused by thermal expansion and contraction, salinity, winds and ocean currents, and other factors, an additional adjustment for Ike is applied for a total adjustment of 0.28 m [*Hope et al*., 2013].

### 2.4. Tidal Forcing

[22] The principal tidal constituents forced in the study are $K_1$, $O_1$, $P_1$, $Q_1$, $M_2$, $K_2$, $N_2$, and $S_2$. The associated periods, tidal potential constants, and earth elasticity factors are the same used by *Kerr et al*. [2013a]. The tidal validation time-dependent astronomical arguments used for the tides-only runs are for a 220 day simulation beginning on 19 May 2008. The time-dependent coefficients used for the Ike hindcast studies match those used by *Kerr et al*. [2013a] for the ULLR mesh and by *Hope et al*. [2013] for the SL18TX33 mesh. The ULLR has open ocean boundaries along the Yucatan Channel and Florida Straits, and the SL18TX33 open ocean boundary is located along the 60°W meridian. The ULLR forcing matches that used by *Kerr et al*. [2013a], and the SL18TX33 forcing matches that used by *Hope et al*. [2013].

[23] A comparison of the *EC2001v2e* [*Mukai et al*., 2002], *FES2004* [*Lyard et al*., 2006], *FES95.2* [*Le Provost et al*., 1994, 1995], and *OSU TPXO7.2* [*Egbert et al*., 1994; *Egbert and Erofeeva*, 2002] tidal atlases showed the utility of placing an open ocean boundary at the 60°W meridian as opposed to along the Yucatan Channel and Florida Straits. Amplitudes vary slightly across each of the tidal atlases at the Yucatan Channel and Florida Straits open ocean boundaries of the ULLR mesh for each of the constituents, whereas the amplitudes and phases for the all the tidal atlases at the 60°W meridian open boundary of the SL18TX33 mesh are in good agreement. A preliminary examination found that using the *EC2001v2e* tidal atlas for the ULLR open ocean boundary forcings was most appropriate.

### 2.5. Meteorological Forcing

[24] This study used the same meteorological forcing and methodology to hindcast Ike that was described by *Kerr et al*. [2013a] for the ULLR mesh and by *Hope et al*. [2013] for the SL18TX33 mesh. Structured data assimilated wind and pressure fields were provided by OceanWeather Inc., and as in the previously mentioned studies, this study applied a data-driven sector-based wind drag law [*Powell et al*., 2003; *Powell*, 2006; *Dietrich et al*., 2011a] to compute drag coefficients for both ADCIRC and SWAN. No meteorological forcing was applied for the tidal simulations.

### 2.6. ADCIRC Bottom Friction

[25] This study uses the Manning's *n* bottom friction formulation for ADCIRC. ADCIRC is internally equipped with three parameterizations of bottom friction: a hybrid quasi-linear Chezy formulation [*Mukai et al*., 2002], Manning's *n* formulation [*Bunya et al*., 2010; *Martyr et al*., 2013], and the Chezy formulation. Bottom stress is applied via a quadratic slip condition:

$$\frac{\tau_{bx}}{\rho_0} = C_f U \sqrt{U^2 + V^2} \tag{1}$$

$$\frac{\tau_{by}}{\rho_0} = C_f V \sqrt{U^2 + V^2} \tag{2}$$

where $C_f$ is the bottom drag coefficient, $\rho_0$ is the density, and $U$ and $V$ are the depth-averaged velocities in the $x$ and $y$ directions, respectively. Manning's drag coefficient formulation is:

$$C_f = \frac{gn^2}{\sqrt[3]{H}} \tag{3}$$

where $g$ is the gravitational constant, $n$ is Manning's roughness, and $H$ is the water column height.

[26] Computations presented in this paper use Manning's *n* formulation implemented without and with a lower limit on the bottom drag coefficient (hereafter referred to as the standard and limited Manning's simulations, respectively) to compare its effect on tidal and hurricane-generated water levels and currents across the Louisiana-Texas coast. The use of a lower limit on the bottom drag coefficient imitates the Chezy formulation for deeper water, due to its nondependence on depth. A Manning's formulation with a lower limit of $C_f = 0.003$ is used in the limited Manning's case. The depth at which the limit is applied varies for different Manning's $n$ values (supporting information Figure S1). Essentially, the drag coefficient for $n = 0.012$ in depths greater than 3 m will be forced equal to $C_f = 0.003$ in the limited Manning's simulation, which results in significantly greater friction on the shelf as compared to the standard Manning's simulation.

[27] In ADCIRC, Manning's *n* coefficients for land are spatially assigned (supporting information Figure S2) using land cover information from the databases mentioned by *Dietrich et al*. [2011a]. The spatial representation of Manning's *n* coefficients was specified for all water bodies by correlating values to the bottom surface characteristics. Values for the deep ocean, the LATEX continental shelf, large inland lakes, sheltered estuaries, and straight inlet channels (excluding the Mississippi and Atchafalaya Rivers and their distributaries) are bottom material-dependent and vary between 0.025 and 0.012. Sediment studies of the U.S. continental shelf [*Buczkowski et al*., 2006] reveal a predominantly muddy and silty LATEX shelf and a sandy Florida shelf. Thus, Manning's *n* values were specified as $n = 0.012$ and $n = 0.022$ for the LATEX and Florida shelves, respectively. To account for rougher shorelines, even in cases where lake and shelf bottoms are muddy, *n* values vary between a value of 0.025 at the zero meter contour to the local shelf value (0.012 on the LATEX shelf and 0.022 on the Florida shelf) at depths of 5 m and greater. Manning's *n* values in the deep ocean for depths greater than or equal to 200 m are assigned to 0.012. Riverine Manning's *n* roughness values are dependent on material composition, bed forms, channel shape, and presence of vegetation and can be regime-dependent [*Martyr et al*., 2013]. This is particularly prevalent within the Mississippi River. As such, in the SL18TX33 mesh, Manning's *n* values within the Mississippi River are assigned a base value of 0.022 and increased to 0.025 in regions of significant meandering.

### 2.7. SWAN Bottom Friction

[28] This study considers two bottom friction formulations used in SWAN. Bottom friction in SWAN is a dissipation source term that is dependent on a bottom friction

**Table 2.** Ike Hindcast Specifications for ULLR and SL18TX33 Mesh Resolution Sensitivity Simulations

| | ULLR | SL18TX33 |
|---|---|---|
| Start | 0000 UTC 31 Jul 2008 | 0000 UTC 8 Aug 2008 |
| Meteorology | | Hurricane Gustav<br>Begin: 0000 UTC 26 Aug 2008<br>End: 0900 UTC 4 Sep 2008 |
| | Hurricane Ike | Hurricane Ike |
| | Begin: 1200 UTC 5 Sep 2008 | Begin: 1200 UTC 5 Sep 2008 |
| | End: 0600 UTC 14 Sep 2008 | End: 0600 UTC 14 Sep 2008 |
| Wave friction | $C_{fjon} = 0.19\ m^2/s^3$ | Madsen |

coefficient [*Holthuijsen*, 2007]. It is generally represented as

$$S_{bfr}(\sigma,\theta) = -\frac{C_{bfr}}{g}\left[\frac{\sigma}{sinh(kH)}\right]^2 E(\sigma,\theta)u_{rms,b} \tag{4}$$

where $k$ is the wave number, $C_{bfr}$ is a bottom friction coefficient, $u_{rms,b}$ is the root-mean-square orbital bottom velocity, $E(\sigma,\theta)$ is the directional-dependent and frequency-dependent wave spectrum, and $\sigma$ is the relative frequency of the wave. This study applies two formulations of the bottom friction coefficient: JONSWAP [*Hasselmann et al*., 1973] and Madsen [*Madsen et al*., 1988].

[29] In the JONSWAP model, $C_{bfr}$ is defined as

$$C_{bfr} = \frac{C_{fjon}}{u_{rms,b}} \tag{5}$$

where $C_{fjon}$ is the JONSWAP coefficient. The JONSWAP coefficient is suggested by *Holthuijsen* [2007] to be $0.038\ m^2/s^3$ for swell conditions [*Hasselmann et al*., 1973] and $0.067\ m^2/s^3$ for wind-sea conditions [*Bouws and Komen*, 1983].

[30] The Madsen formulation for the bottom friction coefficient is defined as $C_{bfr} = f_w\sqrt{2}$, where $f_w$ is a nondimensional friction factor dependent on a bottom roughness length scale, $k_N$, and a representative near-bottom excursion amplitude, $a_b$ [*Madsen et al*., 1988]. For hydraulically rough bottoms, where $a_b/k_N < 1.57$, $f_w = 0.3$. For hydraulically smooth bottoms, where $a_b/k_N \geq 1.57$, $f_w$ is estimated with

$$\frac{1}{4\sqrt{f_w}} + \log_{10}\left(\frac{1}{4\sqrt{f_w}}\right) = m_f + \log_{10}\left(\frac{a_b}{k_N}\right) \tag{6}$$

where $m_f$ equals $-0.08$ according to *Jonsson and Carlsen* [1976]. In the SWAN+ADCIRC model, $k_N$ is spatially derived from Manning's $n$ values used by ADCIRC. This is achieved by using the relationship $k_N = 30z_0$, where the bottom roughness length, $z_0$ is defined by *Bretschneider et al*. [1986] as

$$z_0 = H\exp\left[-\left(1 + \frac{\kappa H^{1/6}}{n\sqrt{g}}\right)\right] \tag{7}$$

in which $\kappa$ (Von Karman constant) is equal to 0.41. ADCIRC transmits the water column heights and Manning's roughness values to SWAN so that new roughness lengths can be computed at each SWAN time step [*Dietrich et al*., 2012a]. Whereas ADCIRC has no minimum $n$, this study enforces a minimum Manning's $n$ of 0.02 to be transmitted to SWAN from ADCIRC [*Hope et al*., 2013].

### 2.8. Wave Parameters

[31] For wave simulations using either the ULLR or SL18TX33 meshes, wave direction in the SWAN model is discretized into 36 regular bins. Whitecapping uses the *Komen et al*. [1984] formulation as modified by *Rogers et al*. [2003], and wave breaking due to depth is determined spectrally according to the model of *Battjes and Janssen* [1978] with a breaking parameter of $\gamma = 0.73$ [*Battjes and Stive*, 1985]. Wave frequencies in the simulations using the ULLR mesh are distributed logarithmically into 50 bins with a range from 0.035 to 0.964 Hz, while for the simulations using the SL18TX33 mesh, they are distributed logarithmically into 40 bins with a range from 0.031 to 1.420 Hz. In addition, both the spectral and directional speeds are limited by a Courant-Friedrichs-Lewy condition of 0.25 to limit spurious refractions [*Dietrich et al*., 2012b].

### 2.9. Summary of Simulations

[32] A number of simulations were performed as part of this study to examine model response sensitivities to: (1) mesh resolution, (2) bottom friction formulations used in ADCIRC and SWAN, (3) existence of coastal floodplain inundation, and (4) nonlinear advection, wave radiation stress gradients, and other shallow water equation terms.

[33] Several simulations were performed to address response sensitivities to mesh resolution. Sensitivities to low energy processes, such as tides, were examined by performing 190 day ADCIRC tidal harmonic analyses on the ULLR and SL18TX33 responses. In contrast, high energy processes, such as those found in hurricanes, were examined by performing SWAN+ADCIRC hindcasts of Ike with the ULLR and SL18TX33 meshes. A summary of key model differences for the Ike simulations are provided in Table 2. For the SL18TX33 runs, meteorological forcing for Gustav was applied prior to Ike in order to set ambient water levels in the wetlands. This was not found necessary for the ULLR simulations.

[34] To address model response sensitivities to bottom friction formulation used in ADCIRC, particularly standard versus limited Manning's, tidal harmonic studies and Ike hindcasts were performed without waves for both formulations on the SL18TX33 mesh. To address model response sensitivities to bottom friction formulation used in SWAN, SWAN+ADCIRC Ike hindcasts were performed on the SL18TX33 mesh with the Madsen formulation as used by *Hope et al*. [2013], $C_{fjon} = 0.019\ m^2/s^3$ as used by *Kerr et al*. [2013a], and $C_{fjon} = 0.038\ m^2/s^3$ as recommended by *Hasselmann et al*. [1973].

[35] Tides only and Ike simulations without waves were performed with and without coastal floodplain inundation in order to address model response sensitivities to the existence or nonexistence of attenuating wetting/drying zones. For the case without coastal inundation, low-lying coastal

topography such as wetlands and intertidal flats are defined using raised topographical values at these locations to simulate coastal walls. These raised features replicate scenarios in which land boundaries are used to describe coastlines.

[36] Simulations were also performed to examine the effects of the various dynamical components of the governing equations: specifically, the relative spatial and temporal contributions of the nonlinear advection and wave radiation stress gradient terms. Simulations of Ike with the SL18TX33 mesh were performed with and without each of these components. In addition, the spatial and temporal contributions of all the shallow water equation terms were examined at select geographic points during a hindcast of Ike.

### 2.10. Skill Metrics

[37] To quantify model performance, the following skill metrics were used: coefficient of determination ($R^2$, which describes how well a regression line fits a set of data, with an ideal value of 1), root-mean-square error ($E_{RMS}$, which is a measure of the magnitude of error, with an ideal value of 0), mean error $(\overline{E})$, mean normalized bias ($B_{MN}$, which is a measure of the model's magnitude of overprediction or underprediction normalized to observed value, with an ideal value of 0), standard deviation ($\sigma$), scatter index ($SI$, which is the standard deviation normalized by the mean observed value, with an ideal value of 0), mean absolute error ($MAE$), and mean normalized error ($E_{NORM}$, which is the mean error normalized by the mean observed value, with an ideal value of 0). The equations for mean normalized bias, mean normalized error, and scatter index are:

$$B_{MN} = \frac{\frac{1}{N}\sum_{i=1}^{N} E_i}{\frac{1}{N}\sum_{i=1}^{N} |O_i|} \tag{8}$$

$$E_{NORM} = \sqrt{\frac{\frac{1}{N}\sum_{i=1}^{N} (E_i)^2}{\frac{1}{N}\sum_{i=1}^{N} (O_i)^2}} \tag{9}$$

$$SI = \sqrt{\frac{\frac{1}{N}\sum_{i=1}^{N} \left(E_i - \overline{E}\right)^2}{\frac{1}{N}\sum_{i=1}^{N} |O_i|}} \tag{10}$$

where $O$ is the observed value, $E$ is the error in terms of modeled minus observed, and $N$ is the number of data points [*Hanson et al*., 2009]. Because multiple models' results are being compared to observational data, there is the potential for the models to differ in the number of stations and time series points that are wetted. To counter the potential problem of a disproportionate number of wet and dry points between the models in the statistical analyses, two methods were applied. The first, termed topo-substitution (TS) [*Kerr et al*., 2013a], is the inclusion of all points through a common equalizer, the bathymetry of the model. The bathymetry represents the minimum water level obtainable at any point in the mesh, so dry values were replaced with the ground surface elevation at that location, and a common statistical set was obtained. In the second method, termed wet-only, only those stations or points that wetted were used in each statistical analysis and the rest were omitted.

## 3. Mesh Resolution

[38] To capture low and high energy model response sensitivity to mesh resolution, validations of tides, storm surge, and waves were performed on a moderate-resolution mesh (ULLR) and a high-resolution mesh (SL18TX33).

### 3.1. Tides

[39] The high-resolution SL18TX33 and moderate-resolution ULLR meshes were used to simulate tides over a 220 day period with a start date of 0000 UTC 19 May 2008. These tidal simulations comprised a 30 day spin-up and a subsequent 190 day recording period used for the tidal constituent harmonic decomposition. Model water levels were recorded every half hour at 80 NOAA and 2 International Association for Physical Sciences of the Oceans (IAPSO) Gulf of Mexico stations (Figure 3). Each resulting water level time series was decomposed into 38 individual tidal constituents using T_TIDE [*Pawlowicz et al*., 2002; *Kerr et al*., 2013a].

[40] The eight major tidal constituents $O_1$, $K_1$, $P_1$, $Q_1$, $M_2$, $S_2$, $N_2$, and $K_2$ from the aforementioned decomposition were then compared with the data from the 80 NOAA stations and 2 IAPSO stations. Observed constituent data was compared with modeled constituents from the nearest wet node to a station observation location. Supporting information Figure S3 lists station coordinates and gives the distance in meters between the observed and modeled data points. Due to lack of resolution in some cases, this distance could be on the order of tens of kilometers away. This was much more prevalent for the ULLR mesh than for the SL18TX33 mesh due to the ULLR's coarser resolution.

[41] To investigate tidal response sensitivity to mesh resolution, each station was characterized by geographical location as indicated in Figure 3. The three geographic categories are: open—stations along the nearshore with direct communication to open waters; protected—stations along the nearshore that are in bays or harbors, or are bordered by islands; and inland—stations that are in channels or wetlands.

[42] Figure 4 shows modeled versus observed amplitudes and phases for the full set of tidal constituents at all 82 stations. The error bands for amplitude are equal to half the size of one standard deviation in the observed data of all 82 stations, while for phase, the error bands are equal to 20 degrees. Warmer colors such as yellow and red represent overprediction of the model, while cooler colors such as blue and purple represent underprediction by the model. In comparison with the tidal results of the ULLR simulation, there is a clear and significant improvement in accuracy when using the SL18TX33 high-resolution mesh. For both amplitude and phase, the results from SL18TX33 more accurately match observed data. This is especially clear in tidal amplitude where all of the results are well within two error bands. Both mesh resolutions show some error in phase outside of two error bands; however, the large phase

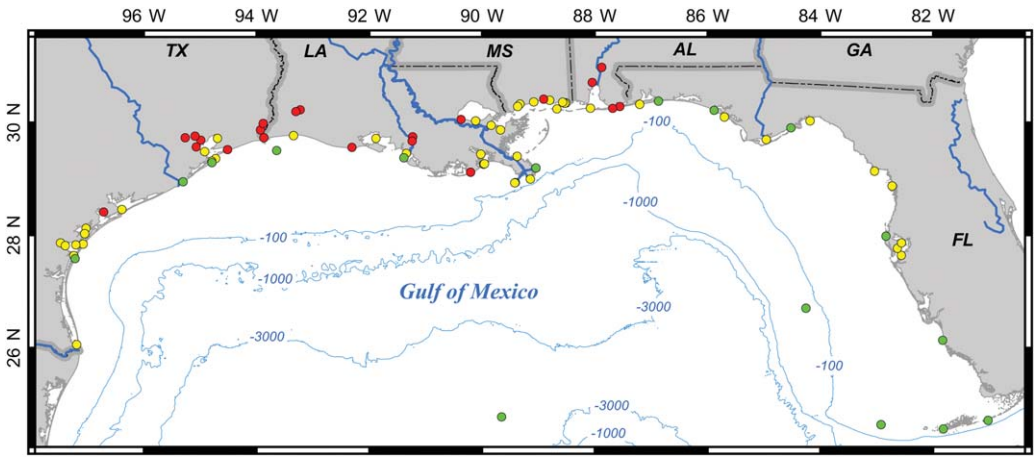


**Figure 3.** NOAA harmonic constituent observation stations categorized geographically as open (green), protected (yellow), and inland (red).

errors for SL18TX33 correlate to the semidiurnal constituents with very small amplitudes along Alabama and eastern Louisiana stations.

[43] Statistical metrics are categorized by constituent and by geographic type as shown in Figure 5. For every constituent, there is an improvement in accuracy as a result

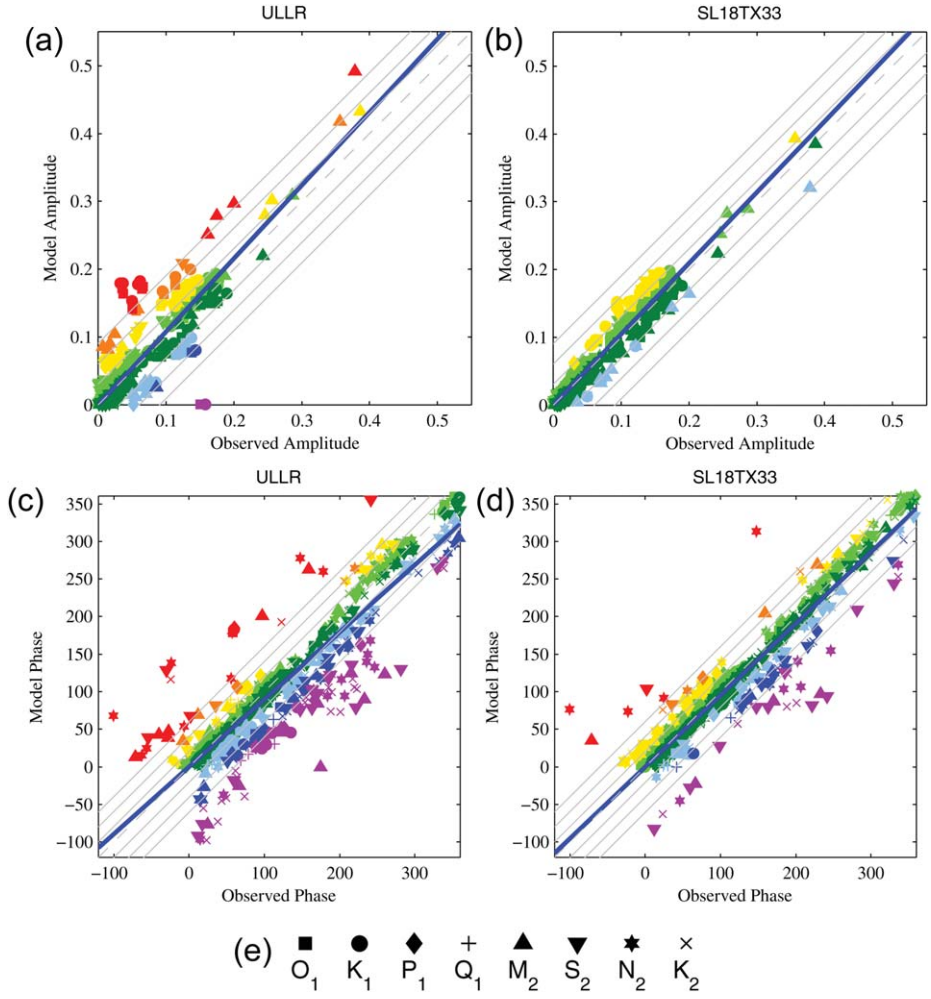


**Figure 4.** Scatter plots of amplitude and phase for ULLR and SL18TX33 tidal harmonic analyses categorized by constituent. Red, orange, yellow, and light green points indicate overprediction; dark green, blue, dark blue, and purple points indicate underprediction. The thick dark blue line represents the best fit zero intercept line.

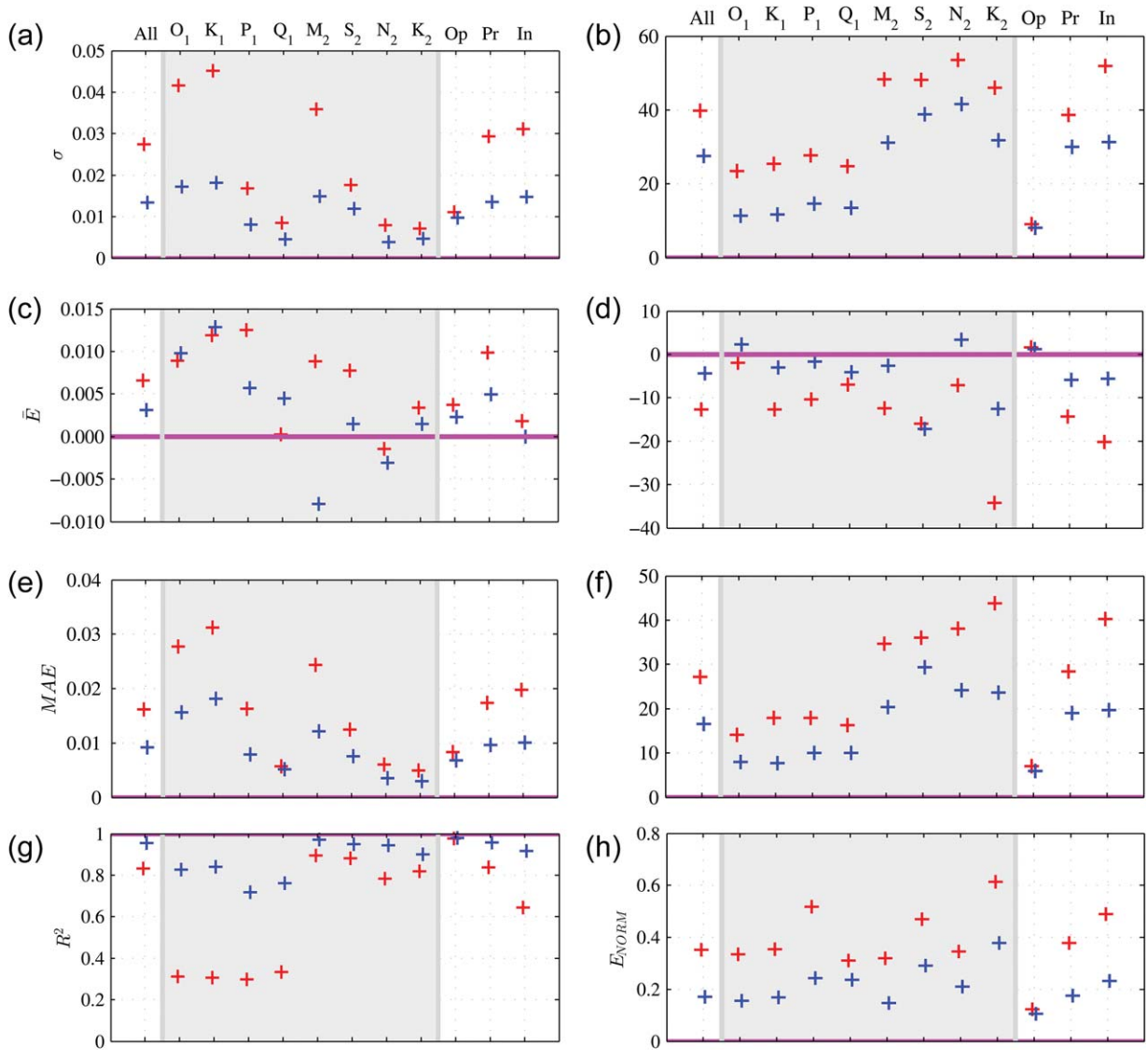


**Figure 5.** Amplitude and phase error statistics categorized by harmonic constituent and geographic type for ULLR (red +) and SL18TX33 (blue +) tidal harmonic analyses. Geographic types are Op: open, Pr: protected, and In: inland.

of higher resolution. Consider the $R^2$ for the amplitudes of the diurnal tides ($O_1$, $K_1$, $P_1$, and $Q_1$) which increase by a factor of 3–4; this improvement in accuracy is not as prominent in the semidiurnal tides due to the larger range in tidal amplitudes of the semidiurnals in comparison to the diurnal constituents. The larger range makes the $R^2$ of the semidiurnal constituents less sensitive to errors. It should be noted that a majority of the stations used in the study are located along the coasts of Louisiana and Texas. Eastern Louisiana is dominated by diurnal tides, while the tides in Texas are mixed diurnal and semidiurnal. This difference causes the statistical metrics to be skewed toward the diurnal tides. Tidal phases are less sensitive to mesh resolution, but an increase in accuracy for all tidal constituents is observed for the SL18TX33 simulation. In general, as seen by $\overline{E}$, the coarser mesh produced a greater phase lag than the higher resolved mesh. In addition, a dramatic improvement was seen for the $K_2$ constituent by using the higher resolved mesh, which has been shown by previous studies, such as *Bunya et al*. [2010] using SL15 (which is more coarse than SL18TX33), to be a very difficult constituent to capture accurately.

[44] Considering geographical location, it is observed that both the SL18TX33 and ULLR simulations were similar and fairly accurate for open stations. Stations categorized as protected or inland were more sensitive to mesh resolution, due to inaccuracies in conveyance and lateral dissipation through inlets, wetlands, and intertidal zones. This is a consequence of coarser resolution not accurately resolving those zones. Statistically, the coarsening of mesh resolution led to an overestimation of tidal amplitudes for stations further inland as well as greater lags in phases.

[45] While the overall statistical analyses of the ULLR and SL18TX33 simulations show a significant increase in accuracy for the higher resolution mesh (see Table 3), Figure 5 demonstrates via geographic categorization, that the

**Table 3.** ULLR and SL18TX33 Tidal Harmonic Analyses Error Statistics

| | Amplitude | | Phase | |
|---|---|---|---|---|
| | ULLR | SL18TX33 | ULLR | SL18TX33 |
| $R^2$ | 0.8333 | 0.9551 | NA | NA |
| $m$ | 1.0804 | 1.0477 | NA | NA |
| $\sigma$ | 0.0274 | 0.0134 | 39.778 | 27.612 |
| $\overline{E}$ | −0.0066 | −0.0031 | −12.676 | −4.407 |
| $MAE$ | 0.0162 | 0.0092 | 27.236 | 16.564 |
| $E_{NORM}$ | 0.3513 | 0.1709 | NA | NA |

bays, estuaries, inland waters, and coastal floodplain require higher resolution and not the Gulf and shelf. This realization can lead to important cost-savings. Furthermore, *Kerr et al*. [2013a] demonstrated that when different ocean circulation models are used for a tidal harmonic decomposition using the same mesh and tidal potential forcing, the results are very similar, thus indicating that tidal model response sensitivity to mesh resolution is likely universal.

### 3.2. Hurricane Ike (2008)

[46] Hindcasts of Ike were performed using SWAN+ADCIRC on the high-resolution SL18TX33 and moderate-resolution ULLR meshes and circulation and wave model response sensitivity to mesh resolution is explored. Model implementation matches descriptions by *Kerr et al*. [2013a] and *Hope et al*. [2013] for the ULLR and SL18TX33 meshes, respectively, and model water levels and wave characteristics were recorded at numerous stations throughout the Gulf of Mexico as also collected by *Kerr et al*. [2013a] and *Hope et al*. [2013].

#### 3.2.1. Wave Characteristics

[47] The effects of mesh resolution on wave modeling were examined via comparison of model results to measured wave parameters in the Gulf and on the Louisiana-Texas shelf. Figure 6 shows the results of significant wave heights for the ULLR mesh (blue line) and SL18TX33 (black line) hindcasts of Ike in comparison to observed data (gray circles). In the deeper waters (>3000 m) of the Gulf (e.g., stations G and J), and on the shelf (50–200 m) (e.g., stations C and K), both models perform similarly and accurately. This is also true for shallower coastal stations along the Louisiana coast (e.g., stations H, I, and J), but not entirely for the coastal stations along Texas (e.g., stations A, B, D, E, and F). Here, a departure between the results can be seen with the higher resolution SL18TX33 mesh appearing to retard the arrival of peak wave heights. The reason for this phenomenon is not clear and further work will be required to identify the cause of this issue. Overall, the ULLR mesh performs comparably to, and in some cases slightly better than, the SL18TX33 model (Figure 6 and Table 4). Results are mixed for wave direction and significant wave height. The SL18TX33 mesh performs better at modeling both peak and mean wave periods, but it must be noted that the difference between the two models is small. These results demonstrate that a moderate resolution wave model can produce comparable wave characteristics in the open Gulf to a much higher resolution wave model, with both offering accurate results.

#### 3.2.2. Water Levels

[48] Figures 7–9 show observed and modeled water level time series at select stations in Texas and Louisiana, for simulations using the ULLR mesh (blue line) and the SL18TX33 mesh (black line). Figure 7 focuses on Galveston Bay and the coast and bays to the southwest of landfall. It is noted that the ULLR mesh does not produce a result at stations N, P, and R. These inland stations were selected to demonstrate both the ability for large surges to propagate inland and into coastal back bays as well as the failure of low-resolution models to capture surge in these areas because the propagation of the surge is primarily conveyed within unresolved hydraulic features. Overall, at open water stations where shore-normal winds resulted in peak surge levels (e.g., stations S, U, V), agreement is seen across both models for peak surge values. This behavior indicates that the ULLR performed comparably to the high-resolution model at open water stations where shore-normal winds were the main surge driver. Also, both models perform comparably before landfall in modeling the forerunner surge, indicating the ULLR mesh is able to capture the geostrophic setup. With the exception of stations L, Q, T, and V, both simulations predict the level of surge with similar accuracy. In the case of station Q, a submesh scale channel is not properly resolved in the SL18TX33 mesh explaining the underprediction of water level prior to landfall; however, once the main surge has propagated overland and overwhelmed the area, the location becomes wetted and the SL18TX33 simulation is able to accurately capture the level of peak surge. Station V is adjacent to the Gulf Intercoastal Waterway (GIWW), to the northwest of Bolivar Peninsula. At this location, the ULLR model is allowing surge to recess too quickly as a result of underconstriction in the GIWW. Similarly, at station L, it is clear that the tidal signal in the ULLR model is too large, implying that too much conveyance is occurring as the tide enters Corpus Christi Bay. In addition, open water stations west of the track (e.g., stations M and O) performed similarly.

[49] The issue of improper conveyance is further demonstrated in Figure 8, in which surge in the channels, lakes, bays, and wetlands of the Texas-Louisiana border and southwestern Louisiana is examined. In this area, the landscape is dominated by low-lying floodplains and marshes. Here, the accurate representation of connectivity between these water bodies is necessary to capture storm surge dynamics. At the open coast (e.g., stations X, Z, and DD), peak surge is similarly and accurately modeled by both meshes; however, further inland, improper conveyance is the primary culprit behind poorly modeled water levels by the ULLR mesh. Station W in Figure 8 lies adjacent to the GIWW, and the peak surge level is modeled accurately by both meshes, but the poor conveyance of the GIWW by the ULLR led to higher water levels prestorm and lower water levels poststorm. Inside the channels, lakes, and bays of southwest Louisiana, the ULLR overestimated peak values of surge (e.g., stations Y, AA, BB, CC, and EE). In contrast, at station FF, too little conveyance causes the station to remain dry prior to landfall in the ULLR mesh, and once it does become inundated, it underpredicts the level of surge. Sometimes, coarser resolution can lead to too much conveyance, and in other cases, it can lead to too little conveyance. The reasons for this vary and relate to resolution,

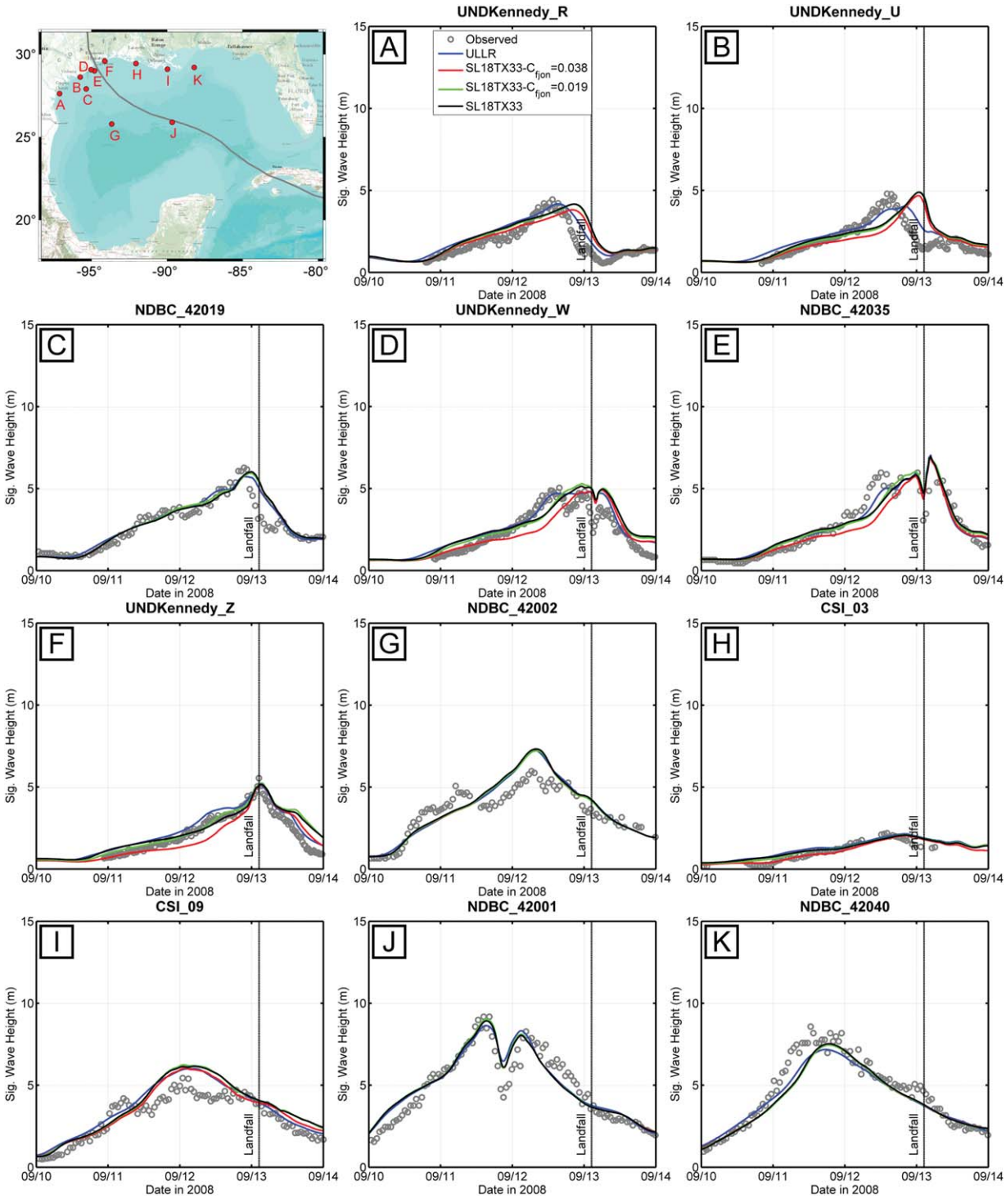


**Figure 6.** Comparison of significant wave height time series at selected stations in the Gulf of Mexico for ULLR (blue), SL18TX33 $C_{fjon} = 0.038$ $m^2/s^3$ (red), SL18TX33 $C_{fjon} = 0.019$ $m^2/s^3$ (green), and SL18TX33 Madsen (black) simulations with observed values (gray circles).

based on the steepness of the topography/bathymetry, the roughness of the landscape, and the size of hydraulic features. For all of the inland stations in this region, the SL18TX33 mesh outperformed the ULLR mesh, demonstrating that higher resolution is necessary to accurately capture the level of surge where resolving hydraulic features is important. Regardless, as each of the stations show (e.g., station K), there is room for improvement by both meshes.

[50] Figure 9 shows stations in the marshes, bays, and rivers of southeastern Louisiana. Similarly to southwestern Louisiana, a complex system of interconnected coastal lakes, bays, and channels are the conduits for inland penetration, meaning an accurate depiction of connectivity and

**Table 4.** Ike Simulation Wave Characteristic and Water Level Hydrograph Error Statistics[a]

| | Model | $R^2$ | $E_{RMS}$ | $\overline{E}$ | $B_{MN}$ | $\sigma$ | SI | MAE | $E_{NORM}$ | #Pts |
|---|---|---|---|---|---|---|---|---|---|---|
| Wave Direction | ULLR | | 45.475 | −6.630 | | 38.884 | 0.242 | 28.776 | | 8 |
| | SL18TX33 | | 42.221 | −3.419 | | 37.253 | 0.217 | 24.891 | | 8 |
| Significant | ULLR | 0.836 | 0.523 | 0.234 | 0.423 | 0.373 | 0.305 | 0.430 | 0.483 | 27 |
| Wave Height | SL18TX33 | 0.766 | 0.569 | 0.215 | 0.271 | 0.469 | 0.290 | 0.440 | 0.372 | 27 |
| Mean Period | ULLR | 0.605 | 11.292 | −5.000 | 0.191 | 8.303 | 0.576 | 7.586 | 0.457 | 19 |
| | SL18TX33 | 0.548 | 12.622 | −5.723 | −0.018 | 9.754 | 0.818 | 7.538 | 0.332 | 19 |
| Peak Period | ULLR | 0.661 | 2.354 | 1.222 | 0.306 | 1.831 | 0.332 | 1.738 | 0.457 | 27 |
| | SL18TX33 | 0.593 | 1.983 | 0.673 | 0.091 | 1.722 | 0.191 | 1.424 | 0.227 | 27 |
| Water Level | ULLR | 0.758 | 0.356 | −0.001 | 0.086 | 0.188 | 0.167 | 0.304 | 0.323 | 505 |
| (Wet-Only) | SL18TX33 | 0.823 | 0.284 | −0.056 | −0.011 | 0.166 | 0.146 | 0.238 | 0.244 | 523 |
| | SL18TX33 (w/o waves) | 0.785 | 0.334 | −0.169 | −0.108 | 0.172 | 0.147 | 0.285 | 0.270 | 517 |
| | SL18TX33 (no advection) | 0.803 | 0.311 | −0.106 | −0.051 | 0.174 | 0.152 | 0.264 | 0.262 | 519 |
| Water Level (TS) | ULLR | 0.713 | 0.649 | 0.235 | 0.317 | 0.235 | 0.228 | 0.593 | 0.622 | 573 |
| | SL18TX33 | 0.765 | 0.537 | 0.182 | 0.237 | 0.187 | 0.171 | 0.491 | 0.515 | 573 |
| | SL18TX33 (w/o waves) | 0.724 | 0.578 | 0.094 | 0.158 | 0.194 | 0.171 | 0.529 | 0.540 | 573 |
| | SL18TX33 (no advection) | 0.745 | 0.558 | 0.143 | 0.203 | 0.194 | 0.176 | 0.512 | 0.530 | 573 |

[a]The rows listed as topo-substitution (TS) use the station bathymetry at stations where it is not wetted by the model, while the rows listed (wet-only) omit any station that is not wetted by the model from the analysis. Certain metrics are not applicable to wave direction. Stations selected differ slightly from *Hope et al*. [2013]. Statistics are calculated at each station for all observed time series data and averaged (unweighted) across all stations. Periods of analysis were 0000 UTC 10 September 2008 to 0600 UTC 14 September 2008 for wave characteristics and 0000 UTC 11 September 2008 to 0600 UTC 15 September 2008 for water levels. #Pts refers to the number of stations used in the analysis.

conveyance is necessary to accurately model water levels. For the ULLR mesh, the trend of accurate open coastal stations and overpredicted or underpredicted inland stations seen in Texas and southwestern Louisiana continues in southeastern Louisiana. At open coastal stations II, KK, LL, OO, RR, and QQ, little difference is seen between the SL18TX33 and ULLR results. However, when examining stations where hydraulic connectivity provides the primary pathway for surge, the ULLR results deteriorate. At stations JJ, MM, NN, and PP, the ULLR simulation underpredicted surge. This is most dramatically seen at station JJ, which is located in the Mississippi River. The reason for this underprediction stems both from poor conveyance and a zero flux upriver Mississippi River boundary condition, demonstrating the importance and relative contribution of resolution and riverine flow in storm surge modeling. Stations PP and MM are positioned in the Biloxi and Caernarvon Marshes, respectively. The ULLR mesh underpredicts at both of these stations, due to the lack of connectivity between the open Gulf and inland marshes, whereas SL18TX33 performs more accurately. Finally, further north at station HH west of Lake Maurepas, improper resolution in Pass Manachac, which connects Lake Pontchartrain to Lake Maurepas, causes the ULLR simulation to overpredict water levels. Again, it is noted that, throughout these stations, the SL18TX33 simulation represents a significant improvement in accuracy for the prediction of water levels and peak surge. In open water locations, both high-resolution and moderate-resolution meshes are able to adequately simulate surge water levels; however, further inland, the higher resolution mesh outperforms the coarser resolution mesh.

[51] A quantitative analysis of the results for all the stations located throughout the domain further illustrates the need for high resolution in capturing inland surge dynamics. Table 4 summarizes a statistical comparison of both simulations. Statistically, the SL18TX33 simulation outperforms the ULLR simulation, but by examining each data source individually, it can be seen that data sources located primarily within open waters performed similarly for both meshes (i.e., CSI, NOAA, AK), whereas data sources located further inland (i.e., CRMS, USGS-DEPL, and USGS-PERM) show a more dramatic difference in performance (supporting information Figure S4). For a detailed description of each data source, see *Hope et al*. [2013]. It is also important to note the effect of using wet-only versus topo-substitution (TS) statistical analyses. Whereas the wet-only method shows a negative $B_{MN}$ for USGS-PERM stations, the TS method shows a highly skewed positive $B_{MN}$. This means that in general, the mesh elevations around the USGS-PERM stations were too high, likely on account of coarseness, leading to a nonprediction of low surge levels and an underprediction of high surge levels.

[52] As shown in Table 4, the SL18TX33 mesh has a higher coefficient of determination ($R^2$), a lower error in most metrics ($E_{RMS}$, $MAE$, and $E_{NORM}$) and a lower standard deviation in the error ($\sigma$). In addition, the higher resolution simulation had a better range of inundation as seen by the number of observation stations wetted (# Pts).

### 3.2.3. Maximum Levels

[53] Figure 10 and Table 5 show the meshes' abilities to accurately model peak still-water water levels (high water marks, abbreviated as HWMs). Figure 10 plots the correlation of measured and modeled data. Statistical analyses of high water marks show that the SL18TX33 model outperforms the ULLR model in all facets. The SL18TX33 shows great improvement in correlation between measured and

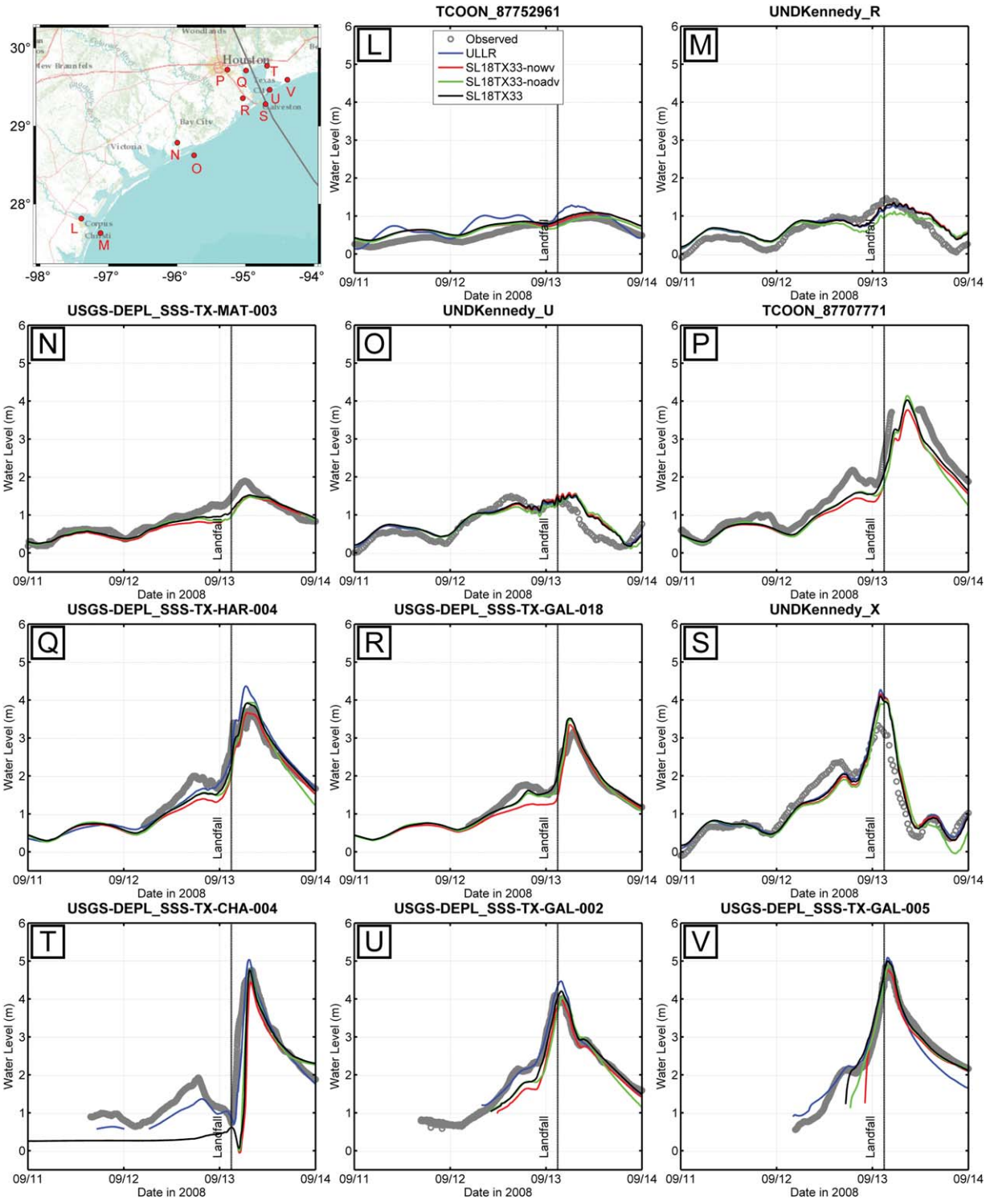


**Figure 7.** Comparison of Ike water level time series at selected stations along the Texas coast ranging from Corpus Christi to Galveston Bay for ULLR (blue), SL18TX33 without waves (red), SL18TX33 without advection (green), and SL18TX33 Madsen (black).

modeled HWMs with an $R^2_{TS}$ value of 0.7 as opposed to an $R^2_{TS}$ value of 0.57 as with the ULLR simulation. Overall, a statistical analysis of HWMs for the ULLR and SL18TX33 simulations further demonstrates the importance of using high resolution in inland areas (see Table 5).

[54] As shown in Figure 11, HWM accuracy is much better for the SL18TX33 simulation throughout the domain, in particular in the regions of northeastern Texas and western Louisiana. Spatially, the Ike-simulated maximum water levels show that the ULLR model produced higher inland

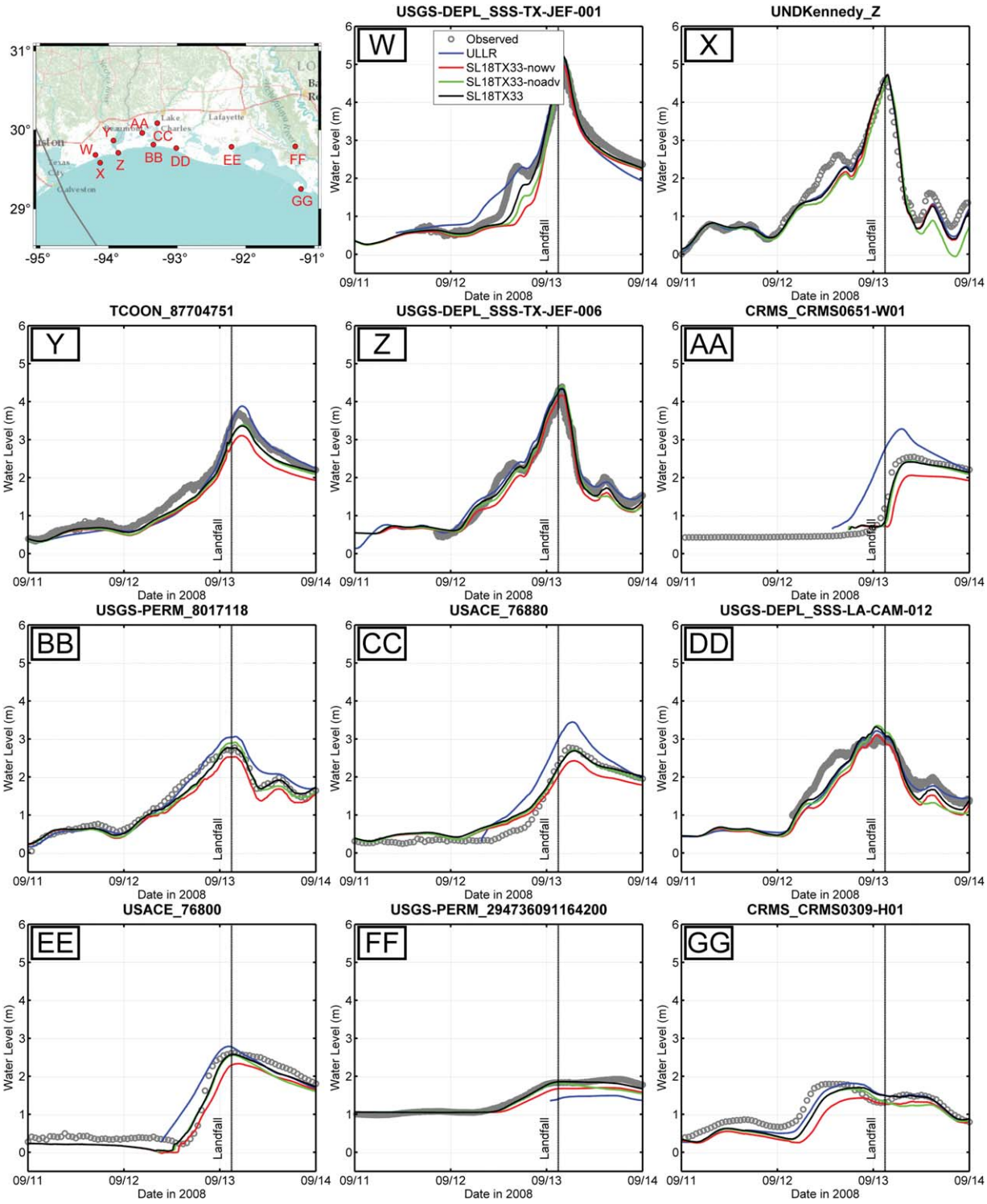


**Figure 8.** Comparison of Ike water level time series at selected stations along the Texas and Louisiana coasts ranging from Galveston Bay to the Atchafalaya Delta for ULLR (blue), SL18TX33 without waves (red), SL18TX33 without advection (green), and SL18TX33 Madsen (black).

water levels than the SL18TX33 model did overland and near the coast, whereas SL18TX33 with its improved resolution of hydraulic features such as bays, channels, and rivers resulted in higher water levels further inland where these connections mattered (e.g., a delineation of each mesh's maximum envelope of water at the Houston Ship Channel is shown in supporting information Figure S5). This image demonstrates the higher resolution of the SL18TX33 as well as the lack of resolution (and consequentially, lack of conveyance) inland in the ULLR model.

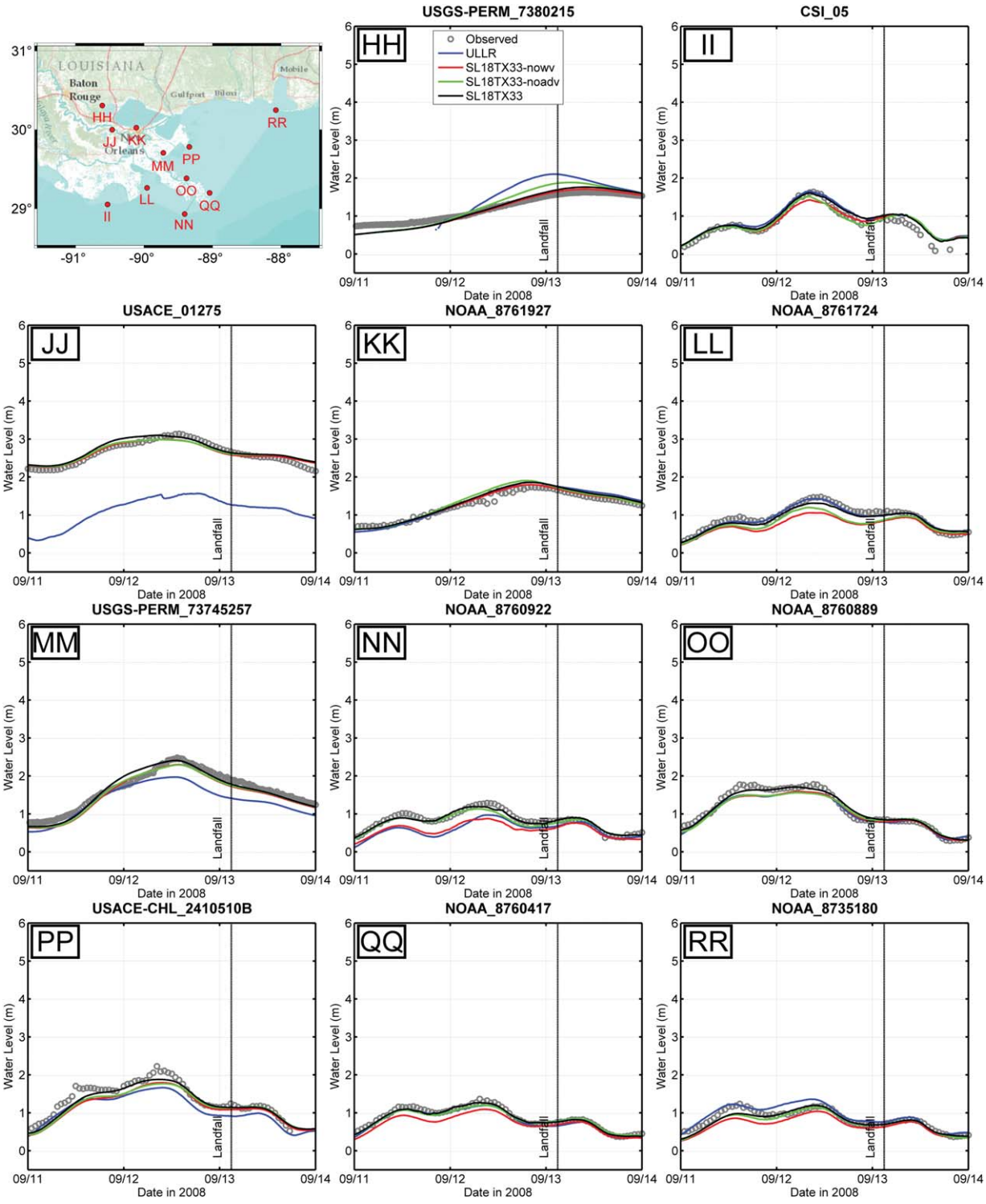


**Figure 9.** Comparison of Ike water level time series at selected stations along the Louisiana and Alabama coasts for ULLR (blue), SL18TX33 without waves (red), SL18TX33 without advection (green), and SL18TX33 Madsen (black).

## 4. Bottom Friction

### 4.1. Energy Dissipation

[55] Model response sensitivity can be highly dependent on the amount of energy being dissipated. Sensitivities to friction and topographic details in the Gulf can behave very differently with low energy processes such as tides compared to high energy processes such as hurricane-driven circulation. An evaluation of tidal energy dissipation due to bottom friction is performed on the high-resolution SL18TX33 mesh. Estimates of maximum nodal dissipation

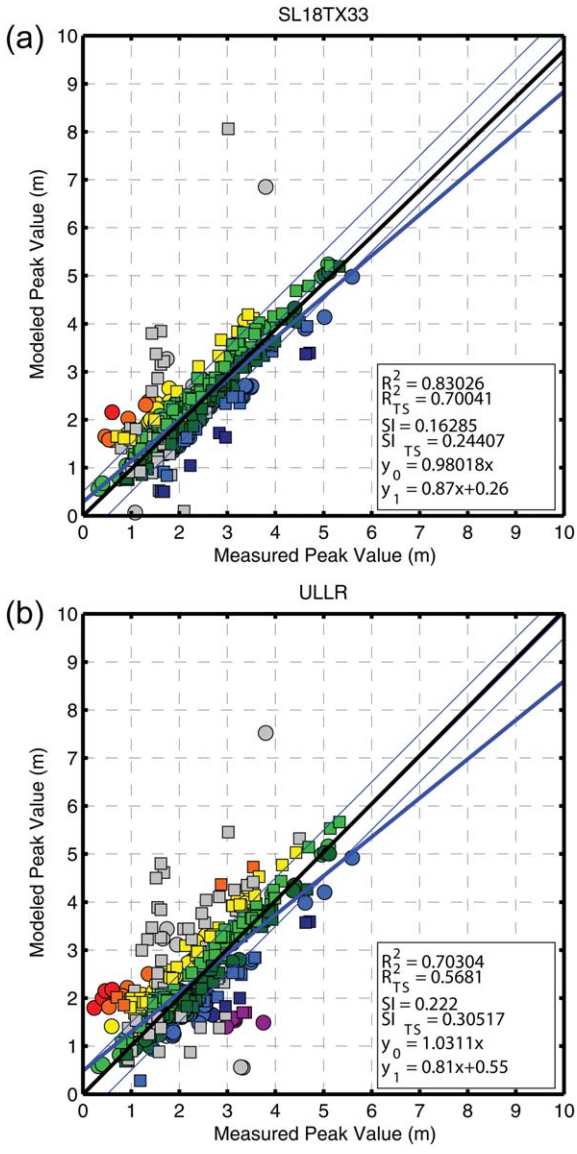


**Figure 10.** Scatter plots of Ike HWMs (circles) and peak hydrograph water levels (squares) for ULLR (left) and SL18TX33 (right). Red, orange, yellow, and light green points indicate overprediction by the model; dark green, blue, dark blue, and purple points indicate underprediction. Green points indicate a match within 0.5 m and gray points indicate locations that were never wetted by the model. Metrics shown are for the wet-only method, unless they have the subscript "TS", which refers to the topo-substitution method. The thick blue line and the thick black line represent the $y_1$ and $y_0$ best fit lines for the wet-only method, respectively.

rates [*Provost and Lyard*, 1997; *Foreman et al*., 1993] are calculated as:

$$D = -\rho \overline{\mathbf{u}} k \mathbf{u_b} \tag{11}$$

where $\rho$ is the ocean density (taken to be 1025 kg/m$^3$), $\overline{u}$ is the depth-averaged velocity, and $k\mathbf{u_b}$ is the bottom stress term:

$$k\mathbf{u_b} = C_f |\mathbf{u}| \mathbf{u_b} \tag{12}$$

[56] By imposing the maximum depth-averaged velocity as the bottom velocity, it is possible to deduce the maximum dissipation of energy due to bottom friction. Dissipation via bottom friction is viewed as the predominant means for tidal dissipation and occurs on continental shelves and within inland waters [*Jayne and St. Laurent*, 2001]. High-resolution meshes can provide insight into localized regions of dissipation and refinements on the total dissipation calculated for such regions [*Zaron and Egbert*, 2006]. Figure 12 shows the maximum velocities and maximum dissipation rates, respectively, across the Louisiana-Texas shelf and inland waters for tides-only and Ike simulations.

[57] For the tidal simulation, maximum currents remain small on the continental shelf and increase to 0.3–0.5 m/s in bays and wetlands. Currents up to 1 m/s occur at the southern edges of the Chandeleur Islands near the Mississippi River Delta and exceed 1 m/s within the Galveston Bay channel that connects to the open ocean. Tidal dissipation rates are negligible on the continental shelf, but increase to 0.5 W/m$^2$ behind barrier islands (e.g., Chandeleur Islands), in bays and confluences with the open ocean (e.g., Vermilion Bay), and in floodplains (e.g., Atchafalaya River floodplain). The largest dissipation rates exceed 1 W/m$^2$ in between the Chandeleur Islands and the Mississippi River Delta, as well as in the southern reaches of Galveston Bay.

[58] In comparison, for the simulation of Ike, the maximum velocities and maximum energy dissipation rates are much higher across the domain, and the areas of high velocities and dissipation rates are no longer restricted to inlets and constricted coastal waters. High energy dissipation rates ranging from 3 to 7 W/m$^2$ are found across the entire broad continental shelf due to a strong shelf current (2–4 m/s). Near Chambers County, Texas, where Ike made landfall, there are also areas of high energy dissipation, which despite low current velocities ($<$1 m/s) are due to the high bottom friction coefficients ($n > 0.1$). In general, these results show that in shelf waters there is a greater degree of sensitivity to bottom friction for high energy processes. Ike's forerunner was highly dependent on the development of a wind-forced, shore-parallel current, which in turn was very dependent on low bottom stress values across the continental shelf. This is especially important when considering bottom friction formulations, because the drag coefficients for deeper waters ($>$3 m) are lower for the standard Manning's formulation than for the limited Manning's formulation.

### 4.2. ADCIRC Bottom Friction

[59] Model response sensitivity to the use of a limited Manning's bottom friction formulation is explored. A tidal simulation and an Ike hindcast were performed on the SL18TX33 mesh with standard and limited Manning's $n$ formulations. The Ike hindcast was performed without tides and waves.

#### 4.2.1. Tides

[60] The methodology for the tidal bottom friction sensitivity study was the same as that performed for the mesh resolution sensitivity portion of this study. Comparisons of

**Table 5.** Ike Simulation HWM Error Statistics[a]

| Method | Model | $R^2$ | $E_{RMS}$ | $\overline{E}$ | $B_{MN}$ | $\sigma$ | SI | MAE | $E_{NORM}$ | #dry | #out | #wet |
|---|---|---|---|---|---|---|---|---|---|---|---|---|
| Wet-Only | ULLR | 0.703 | 0.502 | 0.089 | 0.042 | 0.466 | 0.222 | 0.365 | 0.221 | 68 | 0 | 538 |
| | SL18TX33 | 0.83 | 0.364 | −0.024 | −0.011 | 0.349 | 0.163 | 0.269 | 0.157 | 46 | 3 | 557 |
| TS | ULLR | 0.568 | 0.655 | 0.146 | 0.07 | 0.639 | 0.305 | 0.441 | 0.289 | 68 | 0 | 538 |
| | SL18TX33 | 0.7 | 0.513 | −0.003 | −0.001 | 0.512 | 0.244 | 0.316 | 0.226 | 46 | 3 | 557 |

[a]The rows listed as topo-substitution (TS) use the station bathymetry at stations where it is not wetted by the model, while the rows listed (wet-only) omit any station that is not wetted by the model from the analysis. Because HWMs are single data points, the statistical set included all stations. The number of stations differ slightly from *Hope et al*. [2013] due to an additional filtering technique employed in their study, which would not be suitable here. Stations were tabulated based on whether the station's coordinates were inundated (#wet), not inundated (#dry), or outside the boundaries of the grid (#out).

tidal harmonics categorized by constituent and geographic location are shown in Figure 13. Model performance for each tidal constituent amplitude and phase were comparable between the standard and limited Manning's cases. Both performed reasonably well, with the limited Manning's case having a slightly lower $\overline{E}$ than the standard case, indicating that in water deeper than 3 m, which is the only area where the cases differ, additional damping occurs in the limited Manning's case but is generally minimal. Both case results were categorized by geographic type (open, protected, and inland) as described in the mesh resolution sensitivity portion of this study, and in both cases, model performance for amplitude and phase was found to decrease from open to protected to inland. In addition, the performance for the standard and limited Manning's cases were relatively similar, suggesting that tidal models are not sensitive to a limited Manning's *n* bottom friction formulation. This is reinforced by the overall statistics of these two cases listed in Table 6.

#### 4.2.2. Hurricane Ike (2008)

[61] Differences in maximum Ike water levels and depth-averaged velocities along the Louisiana-Texas coast between the standard and limited Manning's cases are shown in Figure 14. Use of a lower limit on the bottom drag coefficient significantly reduced water levels across the Louisiana-Texas coast for the Ike simulation (Figure 14a). East of the Mississippi River, water levels were reduced by 0.25 m across Breton Sound and the Caernarvon Marsh. Water levels decreased further in Lake Pontchartrain up to 0.5 m. Water levels along the Mississippi River and in the Mississippi River Delta were also reduced by 0.10–0.25 m. Water levels west of the Mississippi River decreased up to 0.5 m in Barataria Bay, Louisiana, with localized reductions in coastal lakes (e.g., up to 0.75 m

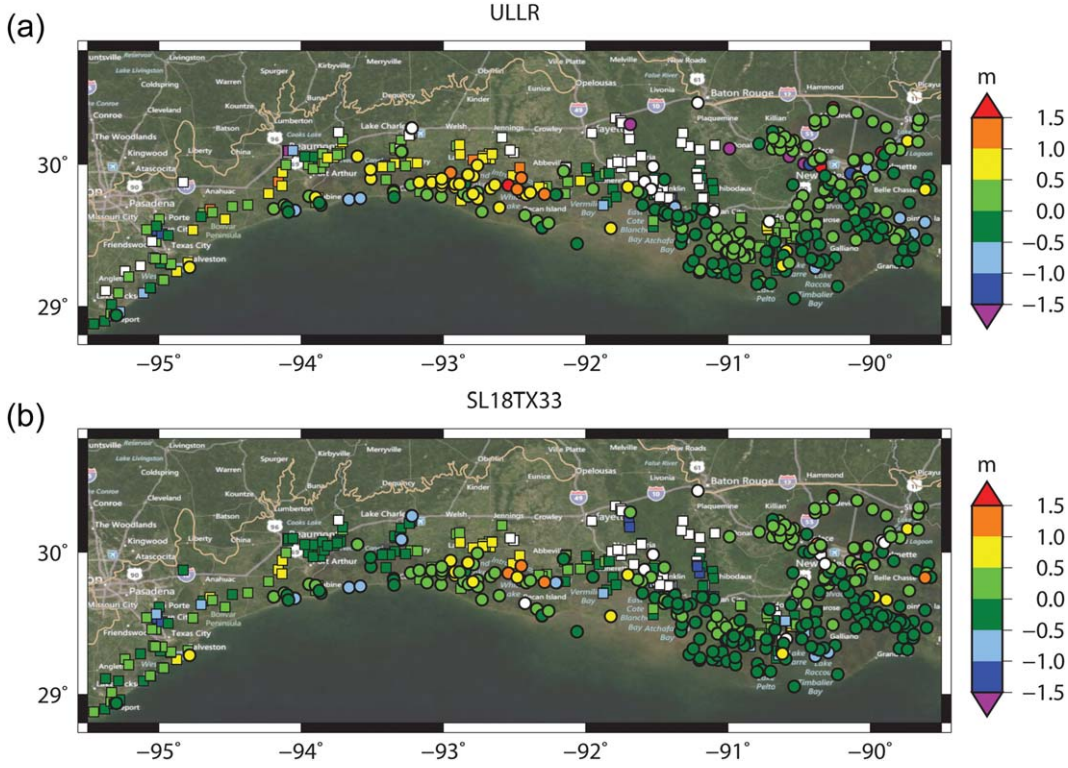


**Figure 11.** Locations of Ike HWMs (circles) and hydrographs (squares) along the northwest Gulf Coast for ULLR and SL18TX33. The points are color-coded to show the errors between measured and modeled peak water levels. Green points indicate matches within 0.5 m and white points indicate locations that were never wetted by the model.

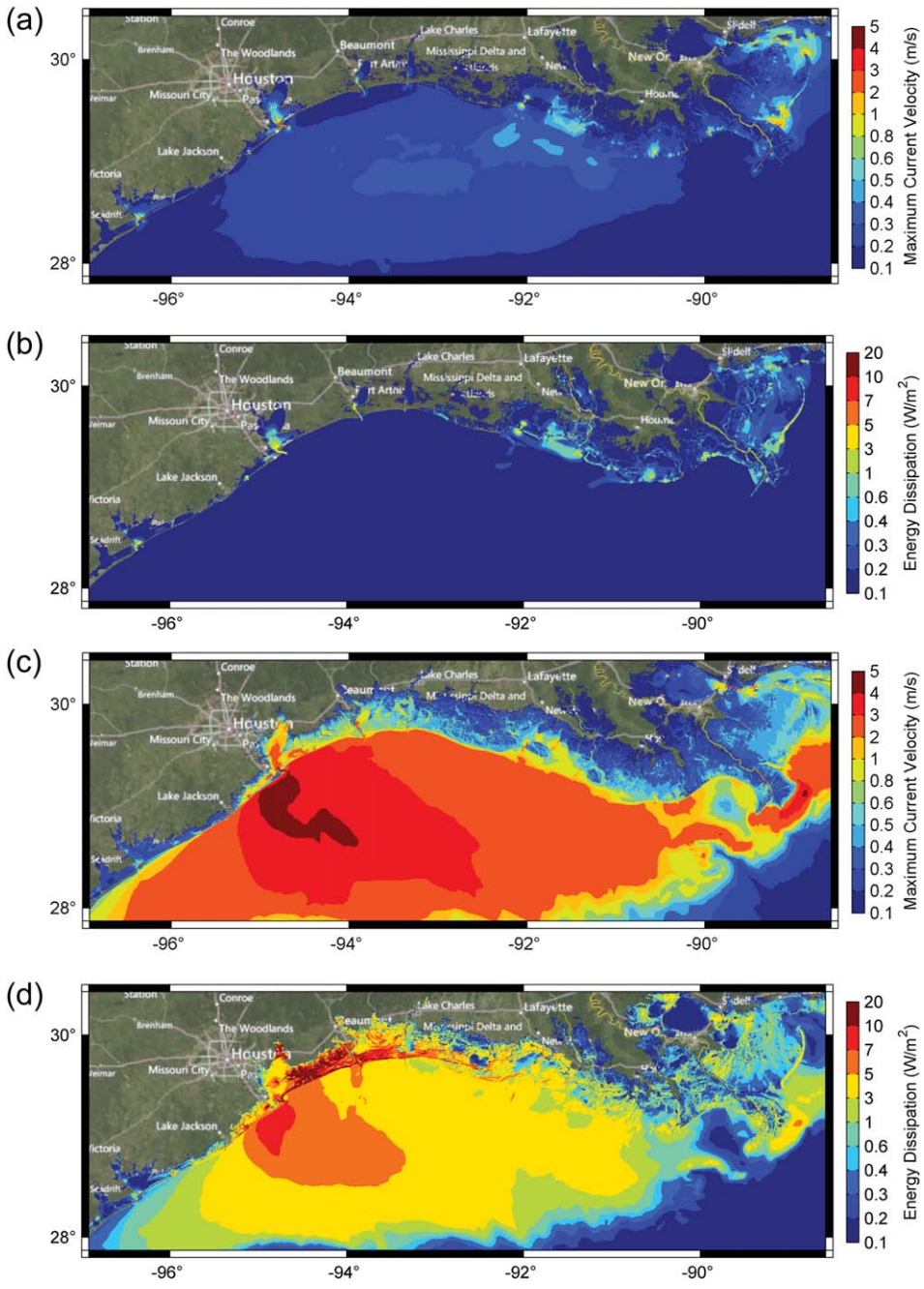


**Figure 12.** Contour plots of (a) SL18TX33 maximum tidal velocities, (b) maximum tidal energy dissipation rates, (c) maximum Ike current velocities, and (d) maximum Ike energy dissipation rates along the northwest Gulf Coast.

near Terrebonne Bay, Louisiana). Use of a lower limit on bottom friction had a larger impact on midshelf and inland waters from western Louisiana to Galveston Bay, Texas. Water levels across the midshelf were reduced by 0.5 m, and water levels inland throughout Galveston, Texas, and Sabine, Texas, were reduced by over 1 m.

[62] Velocities along the shelf were also reduced by the use of the lower limit on the drag coefficient for the Ike simulation (Figure 14b). The impact of the lower limit on the bottom drag coefficient was limited to the continental shelf and shallow waters; no change in water levels or currents is noticed in the deep waters off the continental shelf. Currents near the Mississippi River Bird's Foot were reduced by 1–1.5 m/s, while currents south of the Chandeleur Islands were reduced by 0.5–1 m/s. Currents behind the Chandeleur Islands remained unaffected by the use of a limited Manning's $n$ formulation; however, velocities in narrow channels between islands and within the Rigolets Channel connecting Lakes Pontchartrain and Borgne were reduced by up to 0.75 m/s. Currents across the width of the continental shelf were reduced by the use of the limited Manning's formulation. In western Louisiana, currents

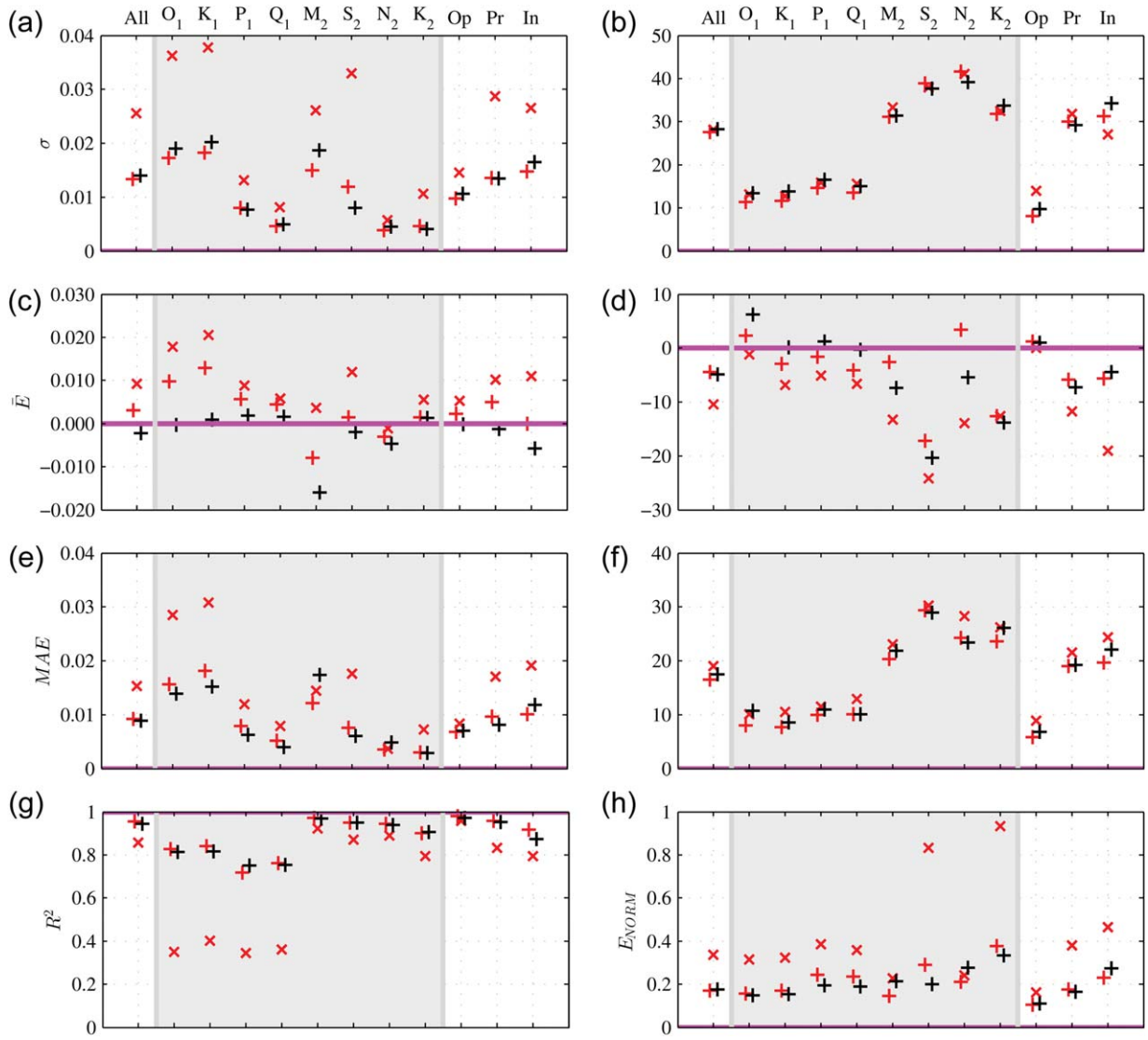


**Figure 13.** Amplitude and phase error statistics categorized by constituent and by geographic type for standard (red +) and limited Manning's (black +) and coastal wall (red ×) tidal harmonic analyses. Geographic types are Op: open, Pr: protected, and In: inland.

were reduced by 0.75–1 m/s in the midshelf and by 0.25–0.5 m/s near the coast. The largest reductions in velocities occurred along Ike's storm track near Galveston, Texas, where velocities decreased by 1–1.75 m/s. Away from the storm track and southwest along the Texas coastline, velocities decreased by 0.75–1 m/s.

**Table 6.** Tidal Harmonic Analyses Error Statistics for Standard and Limited Manning's Bottom Friction Formulation and Coastal Wall Simulations[a]

| | Amplitude | | | Phase | | |
|---|---|---|---|---|---|---|
| Grid | Standard | Limited | Coastal Wall | Standard | Limited | Coastal Wall |
| $R^2$ | 0.9551 | 0.9430 | 0.8578 | NA | NA | NA |
| $m$ | 1.0477 | 0.9574 | 1.1087 | NA | NA | NA |
| $\sigma$ | 0.0134 | 0.0140 | 0.0255 | 27.612 | 28.204 | 28.124 |
| $\bar{E}$ | −0.0031 | −0.0022 | 0.0092 | −4.407 | −4.885 | −10.392 |
| $MAE$ | 0.0092 | 0.0089 | 0.0153 | 16.564 | 17.499 | 19.000 |
| $E_{NORM}$ | 0.1709 | 0.1759 | 0.3352 | NA | NA | NA |

[a]Values shown represent the "All" data set which includes the $O_1$, $K_1$, $P_1$, $Q_1$, $M_2$, $S_2$, $N_2$, and $K_2$ constituents.

[63] The limited Manning's case resulted in much lower velocities and elevations on the shelf. The differences in water surface elevations (Figure 14a) increase from the edge of the shelf to the coastline; this is indicative of a lack of geostrophic setup resulting from too high of a drag coefficient on the part of the limited Manning's formulation. As suggested by *Kennedy et al*. [2011], the geostrophic setup is dependent on the development of a strong shore-parallel current. That current cannot develop if the drag coefficient is too high, as is the case using the limited Manning's formulation. By using the Manning's formulation without a lower limit and a roughness value of $n = 0.012$ to represent the smooth bottom indicative of the LATEX shelf, the drag coefficient is low enough to develop a strong shore-parallel current to power the geostrophic setup of the forerunner seen during Ike.

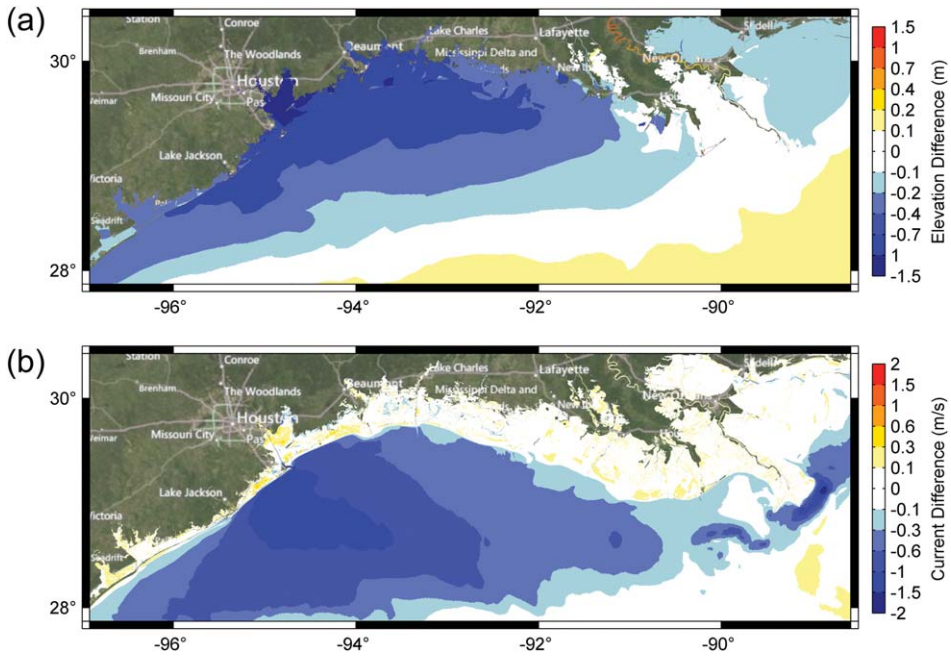


**Figure 14.** Effects of limited Manning's formulation (limited Manning's minus standard) on (top) SL18TX33 maximum water levels and (bottom) maximum current velocities for SL18TX33 Ike along the northwest Gulf Coast.

### 4.3. SWAN Bottom Friction

[64] Ike was hindcast using Madsen and JONSWAP bottom friction formulations in SWAN. Simulations were performed with the JONSWAP formulation, with friction coefficients of $C_{fjon} = 0.019$ m$^2$/s$^3$ and $C_{fjon} = 0.038$ m$^2$/s$^3$, for a total of two JONSWAP runs. $C_{fjon} = 0.038$ m$^2$/s$^3$ is the value suggested by *Hasselmann et al*. [1973] in their study of the North Sea. Significant wave height time series are shown in Figure 6. The green line represents the simulation with $C_{fjon} = 0.019$ m$^2$/s$^3$ and the red line represents the simulation with $C_{fjon} = 0.038$ m$^2$/s$^3$. For swell conditions, the dominant dissipation term outside the breaking zone is bottom friction, while inside the breaking zone it is wave breaking. In general, for wind-sea conditions, the dominant dissipation term in deep waters is whitecapping, in middepth waters it is a combination of whitecapping and bottom friction, and in the breaking zone it is wave breaking. The significant wave height time series shown in Figure 6 cover several days before and after landfall and correspond to periods of both swell and wind-sea conditions. The selected stations include points in deep water, on the shelf, and the nearshore, both near and far from the hurricane track.

[65] Stations G and J are in deep water and show almost no differences between the bottom friction formulations as do stations C and K, which are on the edge of the continental shelf. The other locations, in comparison, are in shallower water and all show differences between the $C_{fjon} = 0.019$ m$^2$/s$^3$ and $C_{fjon} = 0.038$ m$^2$/s$^3$ simulations. In these cases, the higher JONSWAP coefficient value results in lower significant wave heights for the swell portions of the time histories but not as much for the wind-sea portions. For example, swell-dominated station A is far from the storm and the bottom friction is the dominant dissipation term, which is why the $C_{fjon} = 0.038$ m$^2$/s$^3$ run has a lower peak than the $C_{fjon} = 0.019$ m$^2$/s$^3$ run. This is in contrast to station F, which because it is near the track and was dominated at landfall by wind-seas, had identical peak significant wave heights for all bottom friction formulations.

[66] The $C_{fjon} = 0.019$ m$^2$/s$^3$ run produced more accurate significant wave heights than the $C_{fjon} = 0.038$ m$^2$/s$^3$ run, which in general was overly dissipative and produced lower values during swell conditions. A revisit of JONSWAP bottom friction formulation by *Vledder et al*. [2011] found that for sandy bottoms, the value of $C_{fjon} = 0.067$ m$^2$/s$^3$ suggested by *Bouws and Komen* [1983] for wind-sea conditions in the North Sea was too high and that $C_{fjon} = 0.038$ m$^2$/s$^3$ was more appropriate. Because the Louisiana shelf has a smooth muddy and silty bottom in lieu of a rougher sandy bottom, this study of Ike suggests that an appropriate value for the Gulf of Mexico LATEX shelf may be $C_{fjon} = 0.019$ m$^2$/s$^3$ and that future consideration of $C_{fjon}$ values be region-specific and bottom-specific. In contrast to the smooth fine-grain bottom studied here, studies by *Rogers and Holland* [2009] and *Kranenburg et al*. [2011] have shown that under relatively weak waves, fluid mud bottoms, which can vary greatly in rheologic characteristics, can also be highly dissipative and even alter the wave number.

[67] While there was a noticeable difference between the JONSWAP runs, there was very little difference between the Madsen run (black line in Figure 6) and the $C_{fjon} = 0.019$ m$^2$/s$^3$ run. Both formulations showed excellent agreement. Only in nearshore areas was there any discernible difference. For any depths shallower than these nearshore stations, it is expected that wave breaking will become the dominant dissipation term, and therefore it was not determinable if either formulation is more appropriate than the other.

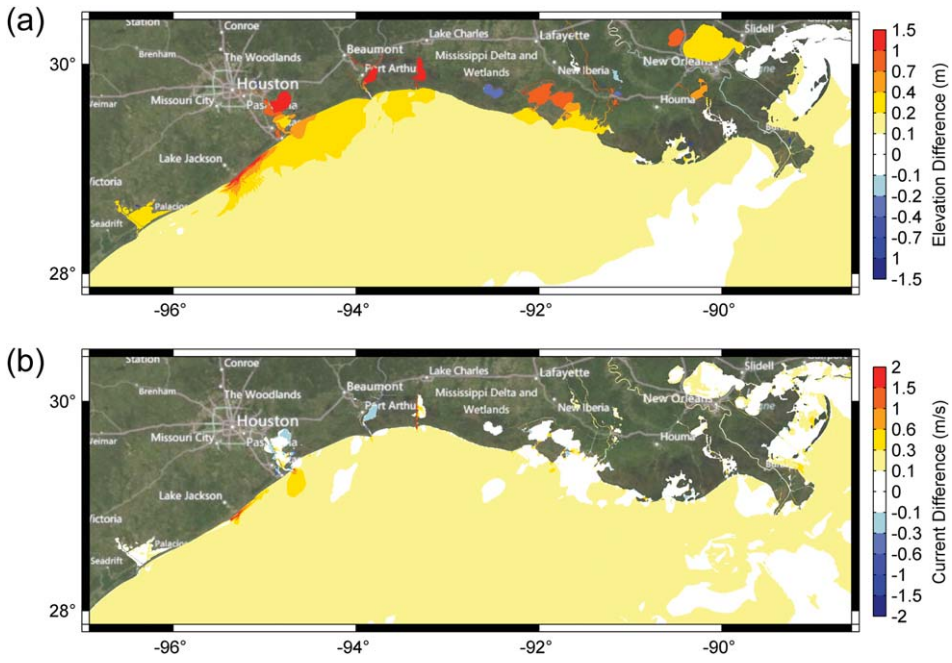


**Figure 15.** Effects of coastal wall (coastal wall minus standard) on (top) maximum water levels and (bottom) maximum current velocities for SL18TX33 Ike along the northwest Gulf Coast.

## 5. Topographic Inundation

[68] The model response to the use of a no normal flow coastline boundary instead of a mesh that features a floodplain which permits inundation is explored here. It is clear that the incorporation of wet/dry logic and a larger mesh to incorporate intertidal zones and the coastal floodplain increases computational cost. The effect that a walled coastline has on model response is explored in detail here. A tidal simulation and an Ike hindcast without waves were performed on the SL18TX33 mesh with the use of an artificial coastline boundary, implemented by the raising of nodal elevations along the coastline and around inland coastal water bodies. The results of these simulations, referred to as the coastal wall simulations, are compared to the results of the standard simulations presented in the mesh resolution section.

### 5.1. Tides

[69] The methods for the tidal harmonic analyses were the same as those performed for the mesh resolution sensitivity portion of this study. Comparisons of tidal harmonics categorized by constituent and geographic location are shown in Figure 13 and tabulated in Table 6. In Figure 13, model performance for each tidal constituent amplitude decreased when intertidal and inundation zones were eliminated and a coastal wall was used. $R^2$ values decreased for all tidal constituents. Illustrated by the $\overline{E}$, the coastal wall case showed a tendency for overprediction of amplitude when compared to both the observed values and the standard case. In addition, the $E_{NORM}$ of the $S_2$ and $K_2$ constituents were significantly higher in comparison to the standard case and when compared to the other constituents. The coastal wall simulation showed good agreement with observed phases and is comparable in performance to scenarios in which the intertidal zone is present, although somewhat lagged relative to the standard case.

[70] Coastal wall results were also categorized by geographic type (open, protected, and inland) as described in the mesh resolution sensitivity portion of this study (Figure 13). For both coastal wall and standard cases, model performance for amplitude and phase was found to decrease from open to protected to inland stations, with errors increasing greater for the coastal wall case than for the standard case. For the open stations, the tidal signals were weakly affected by a no normal flow coastline boundary; however, as the stations progressed further into protected and inland areas, the use of a no normal flow coastline boundary led to worse performance due to greater amplitudes and greater phase lag. These results reinforce the conclusion that tidal models are sensitive to intertidal zones; the overall statistics of the coastal wall and standard cases are listed in Table 6.

### 5.2. Hurricane Ike (2008)

[71] Differences in maximum water levels and maximum depth-averaged velocities along the Louisiana-Texas coast between the coastal wall and standard cases are shown in Figure 15. The coastal wall case primarily changes water levels in the channels, harbors, and bays, with generally little and some moderate change (<0.4 m) seen in water levels along the nearshore, on the shelf, or in the Gulf (Figure 15a), indicating that attenuation does not appear to be an extremely important factor along the coastal front, but more so in coastal lakes and bays.

[72] There is very little difference between the coastal wall and standard cases along the open coast, due to the large supply of water and limiting of inland flux due to friction. Trinity Bay, Sabine Lake, Calcasieu Lake, and Vermillion Bay all see an excess of 1 m of additional surge as a result of a coastal wall. Little or no change is seen in velocities except in channels and behind barriers and

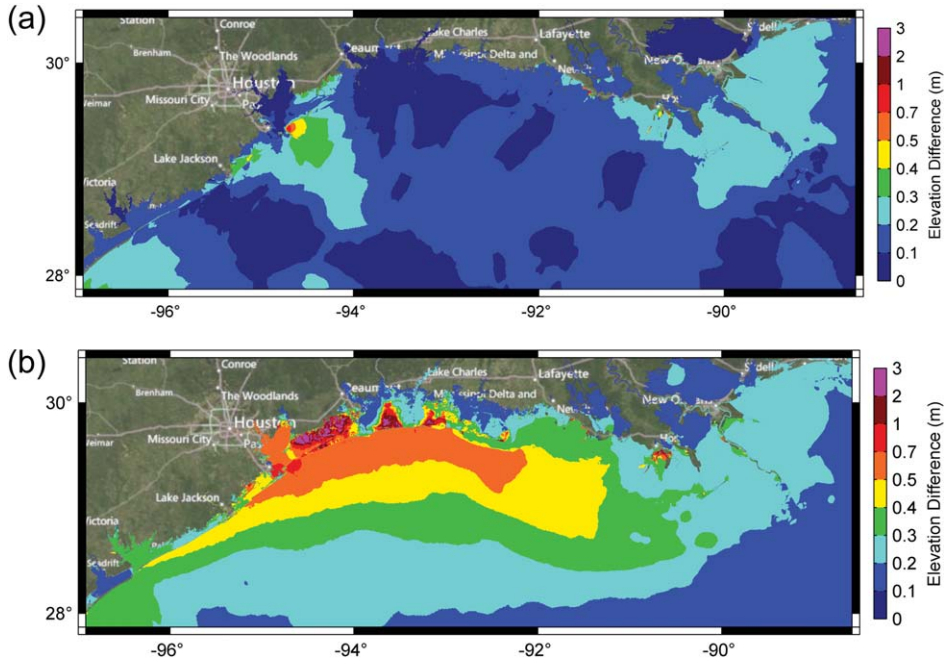


**Figure 16.** Using SL18TX33 for Ike, (top) the effect of advection on maximum water levels and (bottom) the maximum effect of advection on water levels throughout the course of the storm are shown. (bottom) The maximum of differences in water levels at each output step. (top) The difference of the maximum water levels.

islands (Figure 15b). Areas that become the primary conduit of storm surge see increases in velocities, while those areas sheltered by a no normal flow coastline boundary see decreased velocities.

## 6. Contribution of Physical Components

[73] The shallow water momentum equation can be described in terms of its components (*L:* local acceleration, *A:* advection, *C:* Coriolis, *Z:* surface gradient, *P:* atmospheric pressure, *T:* tidal potential, *W:* wind stress, *R:* wave radiation stress gradient, *B:* bottom stress, *D:* diffusion):

$$0 = -\underbrace{\frac{\partial \mathbf{u}}{\partial t}}_{L} - \underbrace{\mathbf{u}\cdot\nabla\mathbf{u}}_{A} - \underbrace{f\times\mathbf{u}}_{C} - \underbrace{g\nabla\zeta}_{Z} - \underbrace{\frac{\nabla p_s}{\rho_0}}_{P} + \underbrace{g\nabla\alpha\eta}_{T} + \underbrace{\frac{\tau_{\mathbf{s,winds}}}{\rho_0 H}}_{W} + \underbrace{\frac{\tau_{\mathbf{s,waves}}}{\rho_0 H}}_{R} - \underbrace{\frac{\tau_{\mathbf{b}}}{\rho_0 H}}_{B} + \underbrace{\frac{\mathbf{M}}{H}}_{D} \tag{13}$$

where **u** represents the depth average velocity, $f$ is the coriolis term, $\zeta$ represents the free surface departure from the geoid, $p_s$ represent the atmospheric pressure at the sea surface, $\alpha$ is the earth elasticity reduction factor, $\eta$ is the Newtonian equilibrium tide potential, $\tau_{s,\text{winds}}$ and $\tau_{s,\text{waves}}$ represent the imposed surface stresses for winds and waves respectively, $\tau_b$ represents the bottom stress, and $M$ represents lateral stress gradients.

[74] This study seeks to identify the relative contributions of these components in a storm surge model so as to improve our understanding of storm surge physics. The driving forces, atmospheric pressure, tidal potential, wind stress, wave radiation stress gradient, and bottom stress, are dependent on the quality of the input and the parameterizations used, whereas the local acceleration, advection, Coriolis, and surface gradient components are only responsive to driving terms.

### 6.1. Advection

[75] A simulation of Ike was performed on SL18TX33 using SWAN+ADCIRC without nonlinear advection terms and the resulting water levels were compared to the SWAN+ADCIRC hindcast that included nonlinear advection terms to determine the relative effect that advection plays on storm surge. Figure 16 (top) shows the difference between maximum water levels of the run with advection and the maximum water levels of the run without advection. Figure 16 (bottom) shows the maximum of the difference between the water levels of the run with advection and the run without advection at each output step of 900 s. These two plots show the contribution of advection from two different perspectives. The first considers the maximum contributions, whereas the second illustrates how that contribution can vary over time. In Figure 16 (top), the contribution of advection to maximum water levels is 0–0.2 m between Corpus Christi, Texas, and the Louisiana-Mississippi border, except along the wetlands bordering the Mississippi River, the southwest Texas continental shelf, and directly around the area where Ike made landfall, which received 0.2–0.7 m of additional water. There is very little difference along the inundated coast for maximum water levels. In contrast, Figure 16 (bottom) shows that at time points during the storm, the contribution of advection leads to an increase of water levels all across the continental shelf and inland areas, with increases as much as 0.7 m along the nearshore and as much 2 m in some

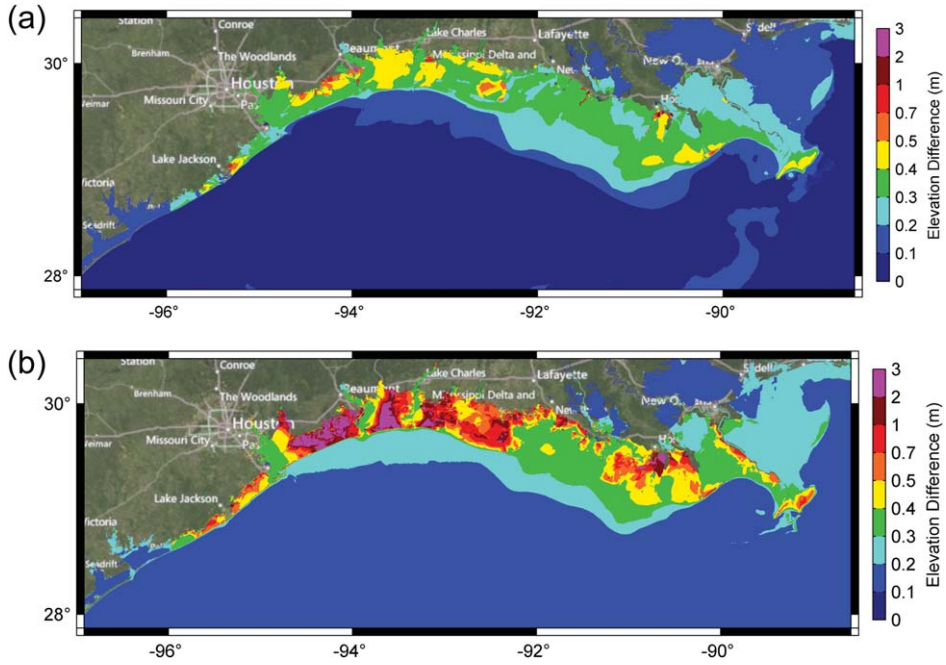


**Figure 17.** Using SL18TX33 for Ike, (top) the effect of wave radiation stress on maximum water levels and (bottom) the maximum effect of wave radiation stress on water levels throughout the course of the storm are shown. (bottom) The maximum of differences in water levels at each output step. (top) The difference of the maximum water levels.

inland inundated areas. These high numbers in the inland areas are a result of the earlier arrival of high water levels resulting from the case with advection.

[76] This difference that occurs in time is due to the importance of the nonlinear advection terms associated with the strong shore-parallel shelf currents that led to Ike's forerunner. The hydrographs presented in Figures 7–9 further illustrate the contribution of the nonlinear advection terms to the geostrophic setup and the resonant shelf waves.

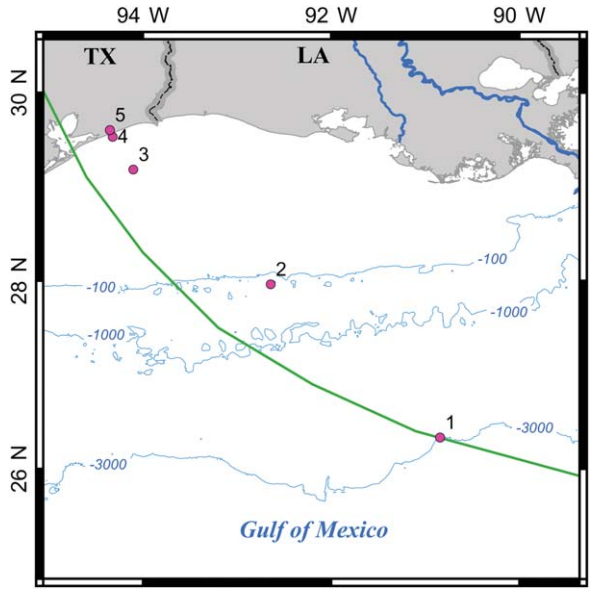


**Figure 18.** Location map of stations being compared in Figure 19.

At location X of Figure 8, advection is responsible for a 10–20 cm increase of water levels in the forerunner and a 30–40 cm increase of water levels in the resonant cross-shelf waves. The advection terms were also found to improve results in wetland areas as illustrated by location MM of Figure 9. In addition, statistical values were better for the case with advection than without (Table 4), reinforcing the importance of the nonlinear advection terms.

### 6.2. Waves

[77] Similar to the analysis of the advection contribution, a simulation of Ike was performed on SL18TX33 using ADCIRC with no wave forcing and the resulting water levels were compared to the SWAN+ADCIRC hindcast that included wave forcing to determine the relative effect that wave radiation stress gradients play on storm surge. Figure 17 (top) shows the difference between the maximum water levels of the run with waves and the maximum water levels of the run without waves. Figure 17 (bottom) shows the maximum of the difference in water levels between the runs with and without waves at each output step of 900 s. These two plots show the contribution of waves in two ways. The first considers the maximum contributions, whereas the second illustrates how that contribution can vary over time. In Figure 17 (top), the contribution of waves to maximum water levels is 0.1–0.5 m along the coastal zone and in the wetlands, although moderately higher in some spots. In contrast, Figure 17 (bottom) shows that at certain times during the storm, the contribution of waves leads to an increase of as much as 2–3 m along parts of the Louisiana-Texas coast, which is due to the earlier arrival of high water levels driven by waves. This effect on overall water levels is reinforced by the results shown in Figures 7–9.

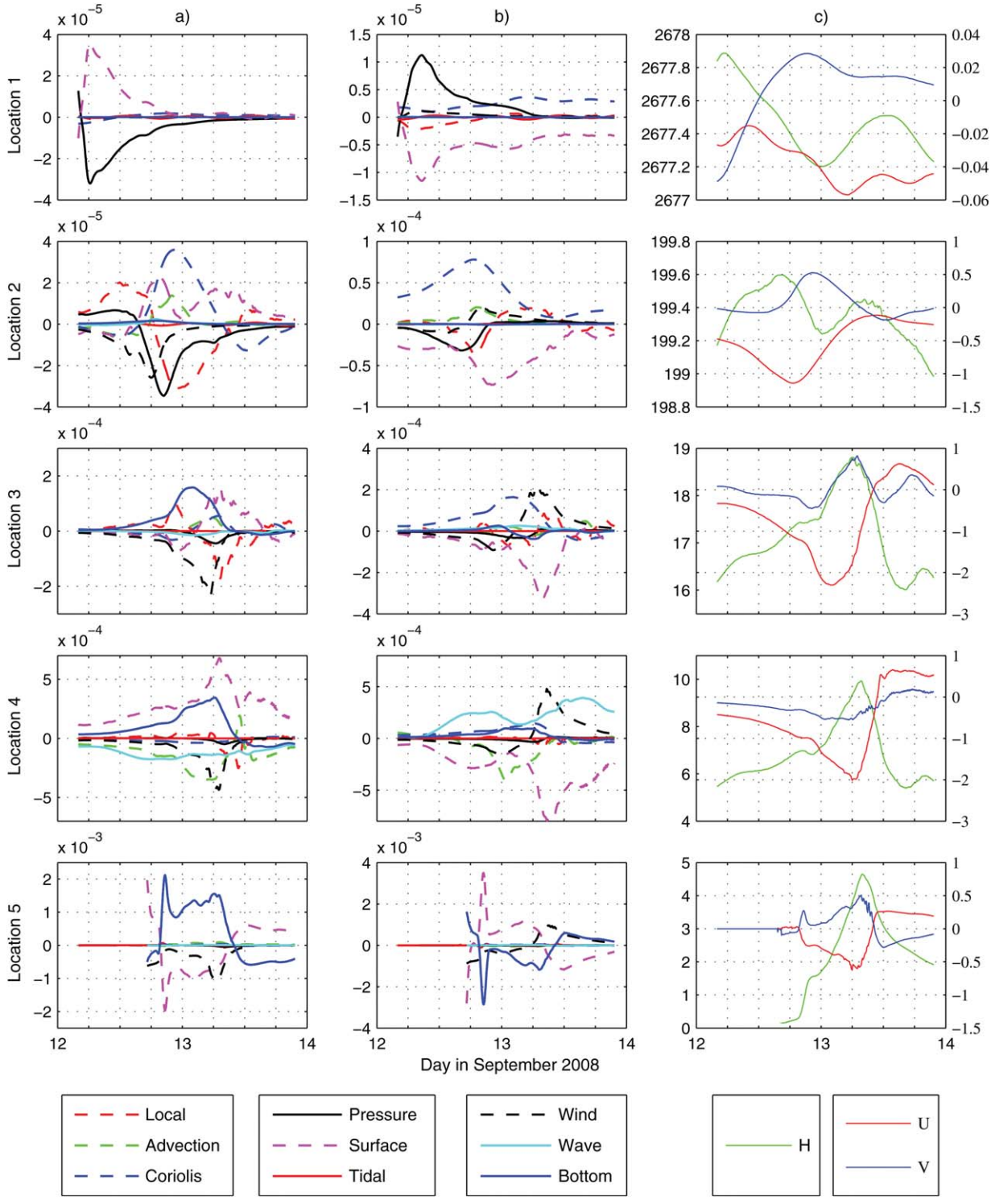


**Figure 19.** Nonconservative shallow water conservation of (a) X-momentum and (b) Y-momentum components in meters per second squared, and (c) elemental average water column height (*H*) (left axis) in meters (NAVD88 2004.65) and elemental average current velocities (*U, V*) (right axis) in meters per second for the five locations shown in Figure 18.

### 6.3. Component Contributions

[78] While the contributions of advection and wave radiation stress gradient terms can be isolated easily in a storm surge model by removing them, the remaining components are more problematic. As an alternative, five locations from the SL18TX33 hindcast of Ike (Figure 18) were selected, and the shallow water equation momentum components were plotted as time series (Figure 19) to summarily

encompass many of the physics modeled. The X-momentum plots are aligned along the west-east axis, with positive values having a west to east direction. The Y-momentum plots are aligned along the south-north axis, with positive values having a south to north direction. These momentum plots are derived elementally and filtered by a Savitzky-Golay scheme to smooth high frequency oscillations [*Savitzky and Golay*, 1964]. Nodal-averaged water surface elevations and current velocities are shown with positive U and V values representing west to east and south to north directions.

[79] Point 1 (−90.84°W, 26.33°N) is located in the deep water (∼2700 m) of the Gulf directly in the path of Ike. The dominant forcing component for both the X and Y axes is the atmospheric pressure gradient, which is primarily balanced by the surface gradient. A striking feature of this plot is the shape of the pressure gradient, which is related to the passage of the storm. The eye of the storm passes over this point around 0500 UTC on 12 September 2008. Although the Coriolis and local terms are evident, the depth-averaged current at this point is less than 10 cm/s, which is why many of the other terms are small, particularly those for bottom friction and advection.

[80] Point 2 (−92.64°W, 27.96°N) is located at the edge of the continental shelf (∼200 m) and approximately 70 km to the right of the hurricane track. The eye of the storm passes closest to this point around 1800 UTC on 12 September 2008. At this depth, the wind stress and pressure components provide relatively similar contributions to the momentum balance. Due to the asymmetry in the wind fields, the wind stress peaks earlier than the pressure gradient. A westward current peaks around 1.2 m/s corresponding to when the eye of the storm is nearest. This leads to the most dominant term, a very strong Coriolis contribution in a northward direction in the Y-momentum equation. A moderately strong Coriolis also develops in an eastward direction in the X-momentum equation. Also seen in both the X-momentum and Y-momentum equations is the advection term which contributes at approximately one-third the scale of the Coriolis term.

[81] Point 3 (−94.1°W, 29.18°N) is located just outside the breaking zone in shallower shelf waters (∼15 m). Here the pressure gradient is no longer strong in comparison to the other terms. The most dominant terms aside from the local and surface terms are wind stress, Coriolis, and bottom friction. Orientation becomes significant at this location due to the proximity to the coastline and the ability for a shore-parallel current to develop. The westward wind stress develops a strong westward current (∼2 m/s) which in turn develops a strong northward Coriolis component. The current is primarily parallel to the coastline and the progression of storm surge onto the coast is much slower, which is why the bottom friction term is much greater in the X-momentum equation than in the Y-momentum equation. The eastward contribution of advection in the X-momentum equation is just as strong as that of the Coriolis term. The strong shore-parallel current is the driver for the Coriolis and bottom friction terms.

[82] Located just off the shoreline in the breaking zone is point 4 (−94.33°W, 29.56°N). The physics at this point are very similar to those at point 3 except that here the wave radiation stress becomes a stronger contributor (directed toward the coastline). Here the Coriolis term is not as major of a contributor. Wind stress, bottom friction, and surface gradient are the major components, with some influence by the advection, Coriolis, and local terms.

[83] Point 5 (−94.35°W, 29.6°N) is located on the shore (∼0 m). Initially a dry element, it becomes wet late on 12 September 2008 and peaks around 4.5 m when Ike made landfall. Due to the shallowness at this location, many of the components are negligible. The major components are wind stress, bottom friction, and surface gradient. This highlights the sensitivity of inundation speed and water levels to parameterization of drag coefficients for wind stress and bottom stress components in these regions.

[84] Atmospheric pressure gradient was a major component in deep water; however, it became inconsequential approaching the shore. The wind stress became important on the shelf and continued to be a major driving force on the shore. Bottom stress was a major dissipative force in shallow water and decreased its contribution approaching deeper water. The wave radiation stress was a contributing force limited to the shallow water breaking zone; it decreased in relative importance further inland and further offshore.

[85] The surface gradient was a major component at all locations and for all directions, while the local acceleration component was moderate only along the shelf where the velocity was affected. Another term affected by velocity was the Coriolis term. Coriolis was a major component on the shelf, particularly because of the strong shore-parallel current that developed for Ike. In addition, advection was a substantial component along the shelf, especially where the shore-parallel currents were larger, which validates its need for inclusion in coastal models.

## 7. Conclusions

[86] This study sought to clarify many of the assumptions and uncertainties that are generally made with coastal and ocean modeling, particularly by addressing model sensitivities to aspects of mesh design, parameterization, and physical components. In particular, coastal and ocean model response sensitivities were examined with respect to: (1) mesh resolution, (2) bottom friction formulations used in ADCIRC and SWAN, (3) use of a no normal flow coastline boundary instead of a coastal floodplain, and (4) the omission of nonlinear advection and waves. Analyses of a tidal harmonics simulation and an Ike hindcast were performed to address both low and high energy processes.

[87] Tidal flows in the Gulf of Mexico contribute to overall water levels and currents in more energetic events such as hurricanes. Tides are a critical first step to validate circulation models used to simulate hurricane events. Tidal validations are important not only to ensure proper handling of regional hydrodynamics, but also because tides contribute to water levels and currents during hurricanes. The Florida shelf on the eastern edge of the Gulf of Mexico and wider parts of the Louisiana-Texas shelf are dominated by mixed diurnal and semidiurnal tides. The tidal regime transitions to predominantly diurnal as one moves into regions where the shelf does not extend as far into the Gulf, such as near the Mississippi River Bird's Foot. While semidiurnal tides are generated by both signal propagation

through the Florida and Yucatan Straits as well as local tidal potential forcing, diurnal tides are dominated by signal propagation through the two straits. Semidiurnal tides are amplified through resonance on the Florida shelf and regions of the Louisiana-Texas shelf, while diurnal tides are relatively homogeneous across the Gulf. Complex low-lying inland topography along the Louisiana-Texas coast plays a significant role in altering tidal signals in inland waters. As such, highly resolved meshes are critical in describing the tidal regime throughout the Gulf, and especially in inland coastal regions.

[88] The SL18TX33 mesh has been validated for tidal amplitudes and phases for the eight dominant tidal constituents at a wide range of open ocean and inland locations throughout the Gulf of Mexico. High model fidelity with NOAA and IAPSO estimated tidal harmonics across geographic types and tidal constituents can be attributed to increased resolution in protected and inland areas, as well as in open coastal regions. In particular, inland regions containing fine-scale topographic features saw a significant increase in accuracy when a high-resolution domain was used. The inability for coarser meshes, such as the ULLR, to accurately capture the conveyance or spatial dissipation in these areas leads to inaccurate modeling of both amplitudes and phases. Tidal flows in deep waters are adequately described with moderate mesh resolution.

[89] Model response sensitivity to mesh resolution was also performed for a SWAN+ADCIRC Ike hindcast. Modeled wave characteristics were similar and accurate for both ULLR and SL18TX33 meshes. At deep-water locations and locations with clear and well-resolved connections to open water, modeled water levels were also similar and accurate for both meshes; however at inland locations, the more highly resolved mesh (SL18TX33) outperformed the moderate-resolution mesh (ULLR). Detailing of fine-scale inland features is necessary for better capture of hurricane surge propagation and attenuation. In regions with long sustained winds, such as in Breton Sound and Caernarvon Marsh, mesh resolution has less impact on overall water levels. However, once hurricane surge has entered the Mississippi River from Breton Sound, high mesh resolution such as that of SL18TX33 is critical in estimating ambient water levels within the river and overall water levels throughout the storm's duration. Coarsely resolved meshes were shown to overestimate river water levels and poorly estimate hurricane surge evolution within riverine environments.

[90] In general, the ULLR's resolution of 8–30 km in the Gulf and 2–8 km of the shelf performed well for tides, waves, and surge, but its resolution of rivers (100–500 m) and floodplain (500–2000 m) was too coarse for adequate inland surge dynamics. For these inland areas, based on its success, the SL18TX33's resolution of 30–80 m for rivers and 80–500 m may be more appropriate ranges for mesh designers to use.

[91] An analysis of the limited Manning's bottom friction formulation (putting a lower limit of $C_f = 0.003$ on the bottom drag coefficient) found that it had little impact on tidal flows but greatly reduced water levels and currents during a hindcast of Ike. Simulations using an Ike wind-forcing and a lower limit on bottom friction reduced water levels by up to 1 m and shelf currents by 1.75 m/s. Use of the limited Manning's formulation dissipated large amounts of energy on the continental shelf, and thus failed to generate Ike's high shore-parallel currents, the related geostrophic forerunner wave, and the associated setup prior to the storm arrival on land, underestimating hurricane-generated water levels by more than 1 m in inland regions.

[92] Ike hindcasts performed with Madsen and JONSWAP bottom friction formulations within SWAN performed similarly and accurately; however, the appropriate JONSWAP friction coefficient to be used for the muddy and silty bottom of the LATEX shelf was found to be $C_{fjon} = 0.019\ \mathrm{m}^2/\mathrm{s}^3$, which differs from recommendations in the literature based on the North Sea. Using the higher values for the North Sea resulted in overly dissipated significant wave heights for swell conditions on the Louisiana-Texas shelf. It is recommended that $C_{fjon}$ be selected based on regional and bottom characteristics.

[93] Absence of a low-lying floodplain leads generally to little or moderate increases ($<0.4$ m) in water levels on the nearshore continental shelf and significant increases in water levels in open and inland bays and estuaries. Wetlands and other low-lying topographic features are shown to provide significant attenuation of tidal signals and some attenuation of hurricane flows. While the use of a coastline boundary and the omission of wet/dry logic does decrease the computational cost of a coastal and ocean model, it results in poor performance for both low and high energy processes in inland regions.

[94] Waves and nonlinear advection are important physical processes that contribute to water levels during a hurricane. For Ike, waves contributed 0.2–0.5 m to maximum water levels along the nearshore and wetlands. Waves also contributed to an earlier arrival of high water levels as part of the forerunner, with some locations, especially near landfall, seeing differences over 1 m. Nonlinear advection contributed 0–0.2 m to maximum water levels along the continental shelf from the Louisiana-Mississippi border to Corpus Christi, with the exception of some areas such as the wetlands bordering the Mississippi River, the southwest Texas continental shelf, and directly around the area where Ike made landfall receiving 0.2–0.7 m. During the storm, nonlinear advection contributed significantly to the geostrophic setup (10–20 cm) and thus resulted in an earlier arrival of high water levels. Nonlinear advection was also essential in capturing the height of the resonant shelf waves, by adding an additional 30–40 cm to water levels. Both waves and nonlinear advection improved statistical model performance. An exploration of SWE components for select locations during Ike gives insight into the relative contributions provided by each of the terms at the deep-water, shelf, nearshore, and floodplain scales, particularly the influence of the Coriolis and bottom friction terms in the development of the strong shore-parallel current that powered Ike's forerunner.

[95] In order to accurately capture the complex and multiscale processes of tides, hurricane surge, and wind waves, it is necessary to model friction correctly and include numerically challenging and costly physical components such as advection and waves because they make a significant improvement. A detailed cost-benefit analysis in terms of relating the degree of accuracy to the cost-savings achieved by using a coastline boundary or coarser

resolution is grounds for further research, but as an initial step, this study identifies how the different approaches affect model accuracy. By using either a coastline boundary or a coarser mesh, model performance compares well along the open coastline to the higher resolution mesh; however, with both tides and hurricane storm surge, performance decreases further into protected and inland areas. A coastline boundary model does not capture intertidal zone attenuation and therefore overpredicts tidal amplitudes in those regions. In addition, resolving inland pathways is necessary for a model to convey the progression of inland surge inundation; by artificial retarding through coarser resolution, a model will overpredict water levels.

[96] **Acknowledgments.** This project was supported by NOAA via the U.S. IOOS Office (awards NA10NOS0120063 and NA11NOS0120141) and was managed by the Southeastern Universities Research Association. In addition, this work used the Extreme Science and Engineering Discovery Environment (XSEDE), which is supported by National Science Foundation grant OCI-1053575.

## References

Battjes, J., and J. Janssen (1978), Energy loss and set-up due to breaking of random waves, paper presented at the 16th International Conference on Coastal Engineering, Hamburg, Germany. Sponsored by ASCE Coastal Engineering Research Council; ASCE Waterway, Port, Coastal and Ocean Division; Ministry for Research and Technology of the Federal Republic of Germany; Free and Hanseatic City of Hamburg; Association for Port and Coastal Engineering; and International Association of the Physical Sciences of the Oceans, ASCE.

Battjes, J., and M. Stive (1985), Calibration and verification of a dissipation model for random breaking waves, *J. Geophys. Res.*, *90*(C5), 9159–9167.

Blain, C., J. Westerink, and R. Luettich Jr. (1994), The influence of domain size on the response characteristics of a hurricane storm surge model, *J. Geophys. Res.*, *99*(C9), 18,467–18,479.

Blain, C., J. Westerink, and R. Luettich Jr. (1998), The influence of domain size on the response characteristics of a hurricane storm surge model, *J. Geophys. Res.*, *26*, 369–401.

Booij, N., R. Ris, and L. Holthuijsen (1999), A third-generation wave model for coastal regions. I- model description and validation, *J. Geophys. Res.*, *104*(C4), 7649–7666.

Bouws, E., and G. Komen (1983), On the balance between growth and dissipation in an extreme, depth limited wind-sea in the southern North Sea, *J. Phys. Oceanogr.*, *104*(C4), 7649–7666.

Bretschneider, C., H. Krock, E. Nakazaki, and F. Casciano (1986), Roughness of typical Hawaiian terrain for tsunami run-up calculations: A users manual, J.K.K. Look Laboratory Report, Univ. of Hawaii, Honolulu.

Buczkowski, B., J. Reid, C. Jenkins, J. Reid, S. Williams, and J. Flocks (2006), usSEABED: Gulf of Mexico and Caribbean (Puerto Rico and U.S. Virgin Islands) offshore surficial sediment data release, U.S. Geol. Surv. Data Ser. 146, version 1.0.

Bunya, S., et al. (2010), A high-resolution coupled riverine flow, tide, wind, wind wave, and storm surge model for southern Louisiana and Mississippi. Part I: Model development and validation, *Mon. Weather Rev.*, *138*(2), 345–377.

Chen C., H. Liu, and R. C. Beardsley (2003), An unstructured grid, finite-volume, three-dimensional, primitive equations ocean model: application to coastal ocean and estuaries, *J. Atmos. Ocean Tech.*, *20*(1), 159–186.

Dawson, C., J. J. Westerink, J. C. Feyen, and D. Pothina (2006), Continuous, discontinuous and coupled discontinuous–continuous Galerkin finite element methods for the shallow water equations, *Int. J. Numer. Methods Fluids*, *52*(1), 63–88.

Dietrich, J., et al. (2010), A high-resolution coupled riverine flow, tide, wind, wind wave, and storm surge model for southern Louisiana and Mississippi. Part II: Synoptic description and analysis of Hurricanes Katrina and Rita, *Mon. Weather Rev.*, *138*(2), 378–404.

Dietrich, J., et al. (2011a), Hurricane Gustav (2008) waves and storm surge: Hindcast, synoptic analysis, and validation in southern Louisiana, *Mon. Weather Rev.*, *139*(8), 2488–2522.

Dietrich, J., M. Zijlema, J. Westerink, L. Holthuijsen, C. Dawson, R. Luettich Jr., R. Jensen, J. Smith, G. Stelling, and G. Stone (2011b), Modeling hurricane waves and storm surge using integrally-coupled, scalable computations, *Coastal Eng.*, *58*(1), 45–65.

Dietrich, J., S. Tanaka, J. Westerink, C. Dawson, R. Luettich, M. Zijlema, L. Holthuijsen, J. Smith, L. Westerink, and H. Westerink (2012a), Performance of the unstructured-mesh, SWAN+ADCIRC model in computing hurricane waves and surge, *J. Sci. Comput.*, *52*, 468–497.

Dietrich, J. et al. (2012b), Limiters for spectral propagation velocities in SWAN, *Ocean Modell.*, *70*, 85–102, DOI: 10.1015/j.ocemod.2012.11.005.

Egbert, G. D., and S. Y. Erofeeva (2002), Efficient inverse modeling of barotropic ocean tides, *J. Atmos. Oceanic Technol.*, *19*(2), 183–204.

Egbert, G. D., A. F. Bennett, and M. G. Foreman (1994), TOPEX/POSEIDON tides estimated using a global inverse model, *J. Geophys. Res.*, *99*(C12), 24,821–24,852.

Foreman, M., R. Walters, and R. Henry (1993), A model for simulating currents in eastern Juan de Fuca Strait and the southern Strait of Georgia, in Proceedings of OCEANS'93. Engineering in Harmony with Ocean, Oceanic Engineering Society, IEEE Council on Oceanic Engineering, Victoria, B.C., vol. C12, pp. 28,629–28,651, doi:10.1109/OCEANS. 1993.325987.

Gouillon, F., S. L. Morey, D. S. Dukhovskoy, and J. J. O'Brien (2010), Forced tidal response in the Gulf of Mexico, *J. Geophys. Res.*, *115*(C10), doi:10.1029/2010JC006122.

Hagen, S. C., J. J. Westerink, R. L. Kolar, and O. Horstmann (2001), Two-dimensional, unstructured mesh generation for tidal models, *Int. J. Numer. Methods Fluids*, *35*(6), 669–686, doi:10.1002/1097-0363(20010330)35:6-669::AID-FLD108-3.0.CO;2-#.

Hanson, J. L., B. A. Tracy, H. L. Tolman, and R. D. Scott (2009), Pacific hindcast performance of three numerical wave models, *J. Atmos. Oceanic Technol.*, *26*(8), 1614–1633.

Hasselmann, K., et al. (1973), Measurements of wind-wave growth and swell decay during the Joint North Sea Wave Project (JONSWAP), *Deutch. Hydrogr. Z. Suppl.*, *A8*(12), 95.

He, R., and R. H. Weisberg (2002), Tides on the west Florida Shelf, *J. Phys. Oceanogr.*, *32*, 3455–3473, doi:10.1175/1520-0485(2002)032-3455:TOTWFS-2.0.CO;2.

Holthuijsen, L. (2007), *Waves in Oceanic and Coastal Waters*, Cambridge Univ. Press, New York.

Jayne, S., and L. St. Laurent (2001), Parameterizing tidal dissipation over rough topography, *Geophys. Res. Lett.*, *28*(5), 811–814.

Jelesnianski, C. P., J. Chen, and W. A. Shaffer (1992), *SLOSH: Sea, Lake, and Overland Surges from Hurricanes*, U.S. Dep. of Commer., Natl. Oceanic and Atmos. Admin., Natl. Weather Serv., Silver Spring, Md.

Jonsson, I., and N. Carlsen (1976), Experimental and theoretical investigations in an oscillatory rough turbulent boundary layer, *J. Hydraul. Res.*, *14*, 45–60.

Kennedy, A. B., U. Gravois, B. C. Zachry, J. J. Westerink, M. E. Hope, J. C. Dietrich, M. D. Powell, A. T. Cox, R. A. Luettich Jr., and R. G. Dean (2011), Origin of the Hurricane Ike forerunner surge, *Geophys. Res. Lett.*, *38*, L08608, doi:10.1029/2011GL047090.

Kerr, P., et al. (2013b), Surge generation mechanisms in the lower Mississippi River and discharge dependency, *J. Waterw. Port Coastal Ocean Eng.*, *139*, 326–335, doi:10.1061/(ASCE)WW.1943–5460.0000185.

Komen, G., S. Hasselmann, and K. Hasselmann (1984), On the existence of a fully developed wind-sea spectrum, *J. Phys. Oceanogr.*, *14*(8), 1271–1285.

Kranenburg, W., J. Winterwerp, G. de Boer, J. Cornelisse, and M. Zijlema (2011), Swan-mud: Engineering model for mud-induced wave damping, *J. Hydraul. Eng.*, *137*(9), 959–975.

Le Provost, C., M. Genco, F. Lyard, P. Vincent, and P. Canceil (1994), Spectroscopy of the world ocean tides from a finite element hydrodynamic model, *J. Geophys. Res.*, *99*(C12), 24,777–24,797.

Le Provost, C., A. Bennett, and D. Cartwright (1995), Ocean tides for and from TOPEX/POSEIDON, *Science*, *267*, 639–642.

Luettich, R., Jr., J. Westerink, and N. W. Scheffner (1992), ADCIRC: An advanced three-dimensional circulation model for shelves, coasts, and estuaries. Report 1. Theory and methodology of ADCIRC-2DDI and ADCIRC-3DL., Dredging Research Program Technical Report DRP-92-6, U.S. Army Engineers Waterways Experiment Station, Vicksburg, MS, 137p.

Lyard, F., F. Lefevre, T. Letellier, and O. Francis (2006), Modelling the global ocean tides: Modern insights from FES2004, *Ocean Dyn.*, *56*(5), 394–415.

Madsen, O., Y. Poon, and H. Graber (1988), Spectral wave attenuation by bottom friction: Theory, paper presented at the 21st International Conference on Coastal Engineering, American Society of Civil Engineers, 978-0-87262-687-4 / 0-87262-687-3, 1989, 3040 pp., 3 vols, Torremolinos, Spain.

Martyr, R., et al. (2013), Simulating hurricane storm surge in the lower Mississippi River under varying flow conditions, *J. Hydraul. Eng.*, *139*, 492–501.

Mukai, A., J. Westerink, R. Luettich Jr., and D. Mark (2002), Eastcoast 2001, a tidal constituent database for western North Atlantic, Gulf of Mexico, and Caribbean Sea, US Army Engineer Research and Development Center, Coastal and Hydraulics Laboratory, Technical Report, ERDC/CHL TR-02-24, 201p. http://www.unc.edu/ims/adcirc/publications/2002/2002_Mukai01.pdf.

Pawlowicz, R., B. Beardsley, and S. Lentz (2002), Classical tidal harmonic analysis including error estimates in MATLAB using T_TIDE, *Comput. Geosci.*, *28*(8), 929–937.

Powell, M. (2006), Drag coefficient distribution and wind speed dependence in tropical cyclones, Final report to the National Oceanic and Atmospheric Administration (NOAA) Joint Hurricane Testbed (JHT) program, Tech. Rep., Atlantic Oceanogr. and Meteorol, Lab., Miami, Fla. http://www.nhc.noaa.gov/jht/05-07reports/final_Powell_JHT07.pdf.

Powell, M. D., P. J. Vickery, and T. A. Reinhold (2003), Reduced drag coefficient for high wind speeds in tropical cyclones, *Nature*, *422*(6929), 279–283.

Provost, C. L., and F. Lyard (1997), Energetics of the M2 barotropic ocean tides: An estimate of bottom friction dissipation from a hydrodynamic model, *Prog. Oceanogr.*, *40*(1), 37–52.

Rogers, E., and T. Holland (2009), A study of dissipation of wind-waves by mud at Cassino Beach, Brazil: Prediction and inversion, *Cont. Shelf Res.*, *29*(3), 676–690.

Rogers, W. E., P. A. Hwang, and D. W. Wang (2003), Investigation of wave growth and decay in the SWAN model: Three regional-scale applications, *J. Phys. Oceanogr.*, *33*(2), 366–389.

Savitzky, A., and M. J. E. Golay (1964), Smoothing and differentiation of data by simplified least squares procedures, *Anal. Chem.*, *36*(8), 1627–1639, doi:10.1021/ac60214a047.

Tanaka, S., S. Bunya, J. Westerink, C. Dawson, and R. Luettich (2011), Scalability of an unstructured grid continuous Galerkin based hurricane storm surge model, *J. Sci. Comput.*, *46*(3), 329–358.

Vledder, G., M. Zijlema, and L. Holthuijsen (2011), Revisiting the JONSWAP bottom friction formulation, Sponsored by ICCE, Coastal Engineering Research Council, Proceedings of the 32nd International Conference Coastal Engineering 2010. Eds., Jane McKee Smith, Patrick Lynett, Shanghai, China.

Westerink, J. J., R. A. Luettich, and J. Muccino (1994), Modeling tides in the western North Atlantic using unstructured graded grids, *Tellus Ser. A*, *46*, 178–199.

Westerink, J. J., R. A. Luettich, J. C. Feyen, J. H. Atkinson, C. Dawson, H. J. Roberts, M. D. Powell, J. P. Dunion, E. J. Kubatko, and H. Pourtaheri (2008), A basin- to channel-scale unstructured grid hurricane storm surge model applied to southern Louisiana, *Mon. Weather Rev.*, *136*(3), 833–864.

Zaron, E., and G. Egbert (2006), Estimating open-ocean barotropic tidal dissipation: The Hawaiian Ridge, *J. Phys. Oceanogr.*, *36*, 1019–1035.

Zhang, Y., and A. M. Baptista, (2008), SELFE: a Semi-implicit Eulerian-Lagrangian Finite-Element model for cross-scale ocean circulation, *Ocean Modelling*, *21*:(3), 71–96.

Zijlema, M. (2010), Computation of wind-wave spectra in coastal waters with SWAN on unstructured grids, *Coastal Eng.*, *57*(3), 267–277.